

# **Experimental and numerical study of mechanical properties of multi-phase medium-Mn TWIP-TRIP steel: influences of strain rate and phase constituents**

J.T. Benzing<sup>1\*</sup>, Y. Liu<sup>2</sup>, X. Zhang<sup>3</sup>, W.E. Luecke<sup>4</sup>, D. Ponge<sup>5</sup>, A. Dutta<sup>5</sup>, C. Oskay<sup>2</sup>, D. Raabe<sup>5</sup>, J.E. Wittig<sup>1</sup>

<sup>1</sup> Vanderbilt University, Interdisciplinary Materials Science, Nashville, TN 37235-1683, USA

<sup>2</sup> Vanderbilt University, Civil and Environmental Engineering, Nashville, TN 37235, USA

<sup>3</sup> University of Illinois at Urbana-Champaign, Aerospace Engineering, 104 South Wright Street Urbana, IL 61801, USA

<sup>4</sup> National Institute of Standards and Technology, Materials Science and Engineering Division, 100 Bureau Drive, Stop 8553, Gaithersburg, MD 20899, USA

<sup>5</sup> Max-Planck-Institut für Eisenforschung, Max-Planck-Str. 1, 40237 Düsseldorf, Germany

\*Corresponding author. Now at the National Institute of Standards and Technology in Boulder, CO. Please contact at: [jake.benzing@nist.gov](mailto:jake.benzing@nist.gov)

## **Abstract**

In the current work we investigate the room temperature tensile properties of a medium-Mn twinning- and transformation-induced plasticity (TWIP-TRIP) steel from quasi-static to low-dynamic strain rates ( $\dot{\epsilon} = 10^{-4}$  s<sup>-1</sup> to  $\dot{\epsilon} = 10^2$  s<sup>-1</sup>). The multi-phase microstructure consists of coarse-grained recovered  $\alpha'$ -martensite (inherited from the cold-rolled microstructure), multiple morphologies of ultrafine-grained (UFG) austenite (equiaxed, rod-like and plate-like), and equiaxed UFG ferrite. The multi-phase material exhibits a positive strain-rate sensitivity for yield and ultimate tensile strengths. Thermal imaging and digital image correlation allow for in situ measurements of temperature and local strain in the gauge length during tensile testing, but Lüders bands and Portevin Le Chatelier bands are not observed. A finite-element model uses empirical evidence from electron backscatter diffraction (EBSD) and transmission electron microscopy (TEM), plus constitutive equations to dissect the microstructural influences of grain size, dislocation density and TWIP-TRIP driving forces on tensile properties. Calibration of tensile properties not only captures the strain rate sensitivity of the multi-phase TWIP-TRIP steel, but also provides opportunity for a complete parametric analysis by changing one variable at a time (phase fraction, grain size, strain-induced twin fraction and strain-induced  $\varepsilon$ -martensite fraction). An equivalent set of high-rate mechanical properties can be matched by changing either the austenite phase fraction or the ratio of twinning vs. transformation to  $\varepsilon$ -martensite. This experimental-computational framework enables the prediction of mechanical properties in multi-phase steels beyond the experimental regime by tuning variables that are relevant to the alloy design process.

## Keywords

Multi-phase steel; medium-Mn steel; twinning and transformation-induced plasticity (TWIP-TRIP); strain rate sensitivity; crystal plasticity finite-element model

## 1. Introduction

Medium-Mn steels balance cost (alloy content and processing) with desired mechanical properties [1,2]. Third-generation advanced high-strength steels (AHSS) consist of an alloying content with a mass fraction of 17 % or less and a multi-phase microstructure ( $\alpha'$  - martensite/ferrite/austenite). An achievable set of mechanical properties for third-generation steels consists of yield strengths greater than 0.5 GPa, ultimate tensile strengths greater than 1 GPa, and uniform elongations equal to or greater than 30 % [1,3–6]. The types of third-generation steels capable of achieving these desired properties are medium-Mn steels, lightweight steels, and quenched and partitioned steels [1,2].

Medium-Mn steels usually contain reverted ultrafine-grained (UFG) austenite, which is formed during intercritical annealing. The partitioning of Mn and C during intercritical annealing (in the  $\gamma + \alpha$  phase field) controls the amount, size, and stacking fault energy of the UFG reverted  $\gamma$  [7,8]. Increasing the intercritical annealing temperature decreases the Mn and C content in austenite and therefore decreases the stacking fault energy (SFE) of the austenite [9,10]. The SFE is important for controlling twinning- and transformation-induced plasticity (TWIP and TRIP) effects in the austenite during deformation [11–16]. Although the primary mode of deformation in austenite is dislocation glide, the predicted SFE of 20 mJ/m<sup>2</sup> has been shown to promote secondary mechanisms (mechanical twinning and/or a transformation to hexagonal  $\epsilon$ -martensite) in coarse-grained austenitic steels [17–25]. Recent work [26] provides more detailed characterization of the microstructural evolution before and after inter-critical annealing for this particular steel composition. Notably, the measured compositions match the equilibrium Thermo-Calc® simulations for austenite and ferrite [27], which predict a room temperature austenite stacking fault energy of 21 mJ/m<sup>2</sup> [26]. Further, the coarse-grained recovered martensite does not completely recrystallize (to form UFG ferrite) and thus partially resembles the cold-rolled state. The small fraction of recovered martensite that recrystallizes does form UFG ferrite, which depends on location within the microstructure (likely near heterogeneous regions of higher dislocation density) and boundary mobility (hindered by Mn decoration of defects and martensite recovery).

Deeper understanding of high strain rate deformation in multi-phase TWIP-TRIP steels is needed to understand the behavior experienced during automotive crashes and during forming operations of complex automotive parts [28]. In a crash, automotive components experience strain rates in the range of  $\dot{\varepsilon} = 10^{-2}$  s<sup>-1</sup> to  $\dot{\varepsilon} = 10^3$  s<sup>-1</sup> [29]. The present work investigates the effects of strain rate (from  $\dot{\varepsilon} = 10^{-4}$  s<sup>-1</sup> to  $\dot{\varepsilon} = 10^2$  s<sup>-1</sup>) on mechanical properties and deformation mechanisms of an ultra-low-C medium-Mn steel. Further, strain rate, temperature, microstructure, composition, and dislocation mobility affect static and dynamic strain-aging in medium-Mn steels [30–40], which can lead to plastic instabilities during deformation and affect strain rate sensitivities of the material. Lüders bands and Portevin-Le Chatelier (PLC) bands, referred to as static and dynamic strain aging effects, are respectively manifested by yield point elongations and serrations in engineering stress-strain curves. Thermal imaging and digital image correlation can be used to reveal the heterogeneous and localized deformation behavior in the gauge sections of tensile specimens [34,41], which can lead to abnormally thin regions in formed automotive parts. The

cold-rolled and annealed medium-Mn steel in this work does not exhibit Lüders banding, mainly due to the grain size and low fraction of UFG ferrite. Another new contribution to the literature is the positive strain rate sensitivity of the ultimate tensile strength for a medium-Mn TWIP-TRIP steel, due in part to the absence of PLC bands, limited elongation, and minimal adiabatic heating.

Multi-scale modeling of medium-Mn steels is an important aspect in alloy design of next-generation multi-phase AHSS. Matlock *et al.* [1] and Gibbs *et al.* [42] predicted areas of opportunity in mechanical properties for third-generation steels by applying Mileiko's composite model [43] to the phase fractions of austenite and  $\alpha'$ -martensite, while Ma and Hartmaier [44] included a martensite nucleation parameter (based on plastic deformation of austenite) to differentiate between the anisotropy of stress-assisted and strain-induced martensitic transformations. A recent trend in advanced high-strength steel design is to employ finite-element modeling to predict deformation and failure mechanisms in multi-phase steels. The finite-element results from a study [45] on a low-C medium-Mn TWIP-TRIP steel revealed an alternating behavior of strain localization. The authors stated that a microstructure-based model helps explain the strain-hardening behavior of medium-Mn TWIP-TRIP steel better than models that don't include initial microstructural inputs. Moreover, microstructure-based finite-element models may ultimately provide answers that sufficiently explain the complex strain-hardening behavior of multi-phase steels and will assist in the design of next-generation advanced high-strength steels [46].

In the present work, a crystal-plasticity finite-element (CPFE) model incorporates a set of constitutive equations to capture the plasticity-enhancing mechanisms in the multi-phase steel including mechanical twinning, phase transformation, forest dislocations, and debris dislocations. A single set of parameters captures the strain rate sensitivity. The experimentally determined microstructural parameters (phase fraction, size, orientation, and deformation mechanisms) are based on EBSD and TEM measurements. A new fundamental contribution to the literature is that the CPFE model enables a systematic parametric investigation of processing-structure-property relationships of the medium-Mn steel beyond the experimental regime by changing a single microstructural variable at a time (phase fraction, grain size, and the ratio of deformation twinning vs. transformation to  $\epsilon$ -martensite). In alloy design, changing only one experimental variable (intercritical annealing temperature) affects multiple microstructural variables (the phase fraction, grain size, transformation rates, and even grain morphology) [2,47–49].

The remainder of this manuscript continues with section 2, which outlines experimental and numerical methods. Section 3 details the experimental and numerical results (including a direct comparison). Section 4 provides discussion relevant to strain rate sensitivity of the multi-phase steel, unique influences of the microstructure on the homogeneous macro-scale deformation, and a parametric analysis for future AHSS design. Section 5 summarizes and concludes.

## 2. Methods

### 2.1 Material

An ingot of the Fe-based alloy (with mass fractions of 12 % Mn, 3 % Al and 0.05 % C) was hot-rolled at 900 °C to 3.4 mm thickness, homogenized in an Ar atmosphere at 1100 °C for 2 h, water-quenched to room temperature, (below the Ms temperature), and cold-rolled to 1.7 mm, (a 50 % reduction in thickness), to produce a deformed martensitic microstructure. The average Vickers micro-hardness value was 390 HV after cold-rolling, (average of 7 indents measured with a load of 2 kg). Dilatometer measurements were carried out under vacuum (specimen dimensions

of 9 mm x 4 mm x 1.7 mm) using a Bähr Dil805 model, equipped with induction heating at 32 kHz. A supply of He was used for the cooling medium. Ac1 and Ac3 temperatures (514 °C and 853 °C) were determined with dilatometer specimens that were heated to 950 °C at 10 °C/s, held for 60 s and cooled at 10 °C/s. The cold-rolled sheets of medium-Mn steel were annealed at 585 °C for 8 h, using a heating rate of 100 °C/s and a cooling rate of 100 °C/s. Following intercritical annealing of the deformed martensitic microstructure at 585 °C, Thermo-Calc®<sup>1</sup> simulations (database: TCFE7) predict a room temperature equilibrium austenite volume fraction of 0.44 and a room-temperature austenite SFE of 21 mJ/m<sup>2</sup>. Since the local microstructure may be strongly influenced by Mn segregation, EDS mapping was performed at low magnification in the SEM on a bulk cold-rolled specimen annealed for 8h at 585 °C, but no Mn-banding or other large-scale segregation was observed. Such phenomena have been observed in hot-rolled medium-Mn steels [50].

## 2.2 Mechanical testing, digital image correlation and thermal imaging

Table 1: Summary of mechanical testing and digital image correlation setup

Rate	Testing machine	DIC Hardware	DIC parameters	Stress measurement
$\dot{\epsilon}=10^{-4} \text{ s}^{-1}$ $\dot{\epsilon}=10^{-2} \text{ s}^{-1}$	Conventional 100 kN servo hydraulic	Lighting: LED Camera: 4MP CMOS Lens: 35mm f11	Pattern: White/rolled black ink Speckle diameter: 15 pixels Scale: 20 pixels/mm Subset: (27 to 33) pixels Step size: (5 to 7) pixels	Conventional load cell
$\dot{\epsilon}=10^1 \text{ s}^{-1}$	High-rate servo hydraulic with slack adapter	Lighting: halogen Camera: 1MP Photron SA5 (256x1024) pixels Lens: 105mm f8	Pattern: White/ rolled black ink Scale: 20 pixels/mm Subset: (29) pixels Step size: (5) pixels	Piezoelectric load cell
$\dot{\epsilon}=10^2 \text{ s}^{-1}$	High-rate servo hydraulic with slack adapter	Lighting: LED Camera: 1MP Photron SA5 (256x1024) pixels Lens: 105mm f8	Pattern: White/black overspray Scale: 15 pixels/mm Subset: (23 to 33) pixels Step size: (1) pixels	Strain gages on specimen head load cell

Table 1 summarizes the testing and optical imaging conditions for the different nominal strain rates. Strain measurement used digital image correlation (DIC) and Correlated Solution Vic-3d software. Each specimen used a nominally  $G=19.8$  mm virtual extensometer centered on the specimen. Forces in the highest rate tests were measured using two strain gages mounted on

---

<sup>1</sup> Certain commercial software, equipment, instruments, or materials are identified in this paper in order to specify the experimental procedure adequately. Such identification is not intended to imply recommendation or endorsement by the National Institute of Standards and Technology, nor is it intended to imply that the equipment or materials identified are necessarily the best available for the purpose.

opposite sides of the upper head of the specimens. These gages were calibrated in situ before the test against the piezoelectric load cell in the testing machine.

Figure S 1 provided in the supplementary material shows the machined tensile specimen used in the servo-hydraulic tests. Specimens used in low-rate tests on the Instron 8502 did not have pin-grip holes. Specimens were water-jet cut from the original steel sheets. Pin-loading holes were milled with a carbide tool while clamped in the vise of a milling machine.

The use of non-contact methods with sufficient data acquisition rates is recommended [51] and allows for in situ measurements of macro-scale strain localizations during tensile testing. Non-contact temperature measurements were collected during tensile testing with an infrared thermal camera (FLIR® A655sc) and ResearchIR™ software. The recording frame rate was varied between 60 Hz (640 pixels x 240 pixels) and 30 Hz (640 pixels x 480 pixels). The calibration range of this device is -40 °C to 150 °C, and within this range the overall accuracy of absolute temperature measurement is  $\pm 3$  °C. The maximum reading that could be displayed outside this calibrated range was 160.2 °C. To ensure consistent temperature measurements, the side of the gauge length without a strain gage was coated with black spray paint (emissivity approximately equal to 1).

### 2.3 Microstructural characterization

EBSD is used to measure grain size distribution, grain morphology, phase fraction and texture evolution before and after deformation. Sections of the material were mounted in conductive Bakelite, and the rolling direction was noted for EBSD sample preparation. These samples were successively ground, auto-polished, etched for 5 s with 5 % Nital to chemically remove mechanical polishing effects, (5 % HNO<sub>3</sub> in 95 % CH<sub>3</sub>OH by volume), and hand-polished using a 50 nm oxide polishing suspension of colloidal silica before being rinsed and blown dry. EBSD measurements were completed using a JEOL JSM-6500F field-emission scanning electron microscope (SEM) with the following parameters: 15 kV accelerating voltage, 12 nA probe current, 18 mm working distance, and a 30 nm step size. Data cleanup with TSL OIM 7 software involved a grain confidence index standardization, and data points with a confidence index lower than 0.1 were omitted from all figures.

Bright-field and dark-field transmission electron microscopy (BF/DF-TEM), convergent beam electron diffraction (CBED), and selected area electron diffraction (SAED) was used to further characterize the UFG structure and deformation mechanisms. TEM-based experiments were performed using an FEI Tecnai Osiris operated at 200 kV. The 3-mm electro-discharge-machined discs were successively ground to 100  $\mu$ m thin and electropolished to electron transparency with a Struers twin-jet system (5 % HClO<sub>4</sub>, 35 % [CH<sub>3</sub>(CH<sub>2</sub>)<sub>3</sub>]-O-C<sub>2</sub>H<sub>4</sub>OH, 60 % CH<sub>3</sub>OH by volume, -30 °C, 15 V).

### 2.4 Crystal plasticity finite-element model

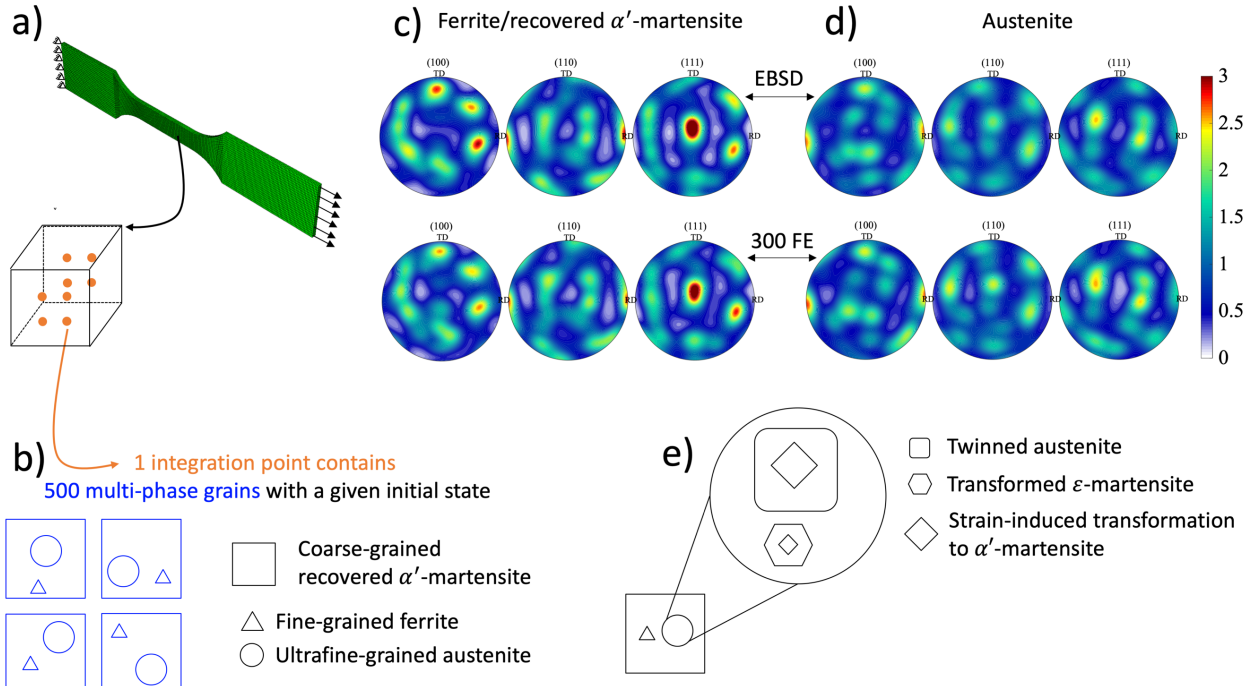


Figure 1: a) Finite-element mesh and boundary conditions of the tensile sample using 30,000 finite-elements (trilinear 8-noded hexagonal elements). b) The generalized plasticity model is summarized for each integration point, which contains 500 multi-phase grains. A comparison of the pole figure orientations measured by EBSD and orientations represented by 300 finite-elements near the center of the gauge length are shown for c) ferrite and the coarse-grained recovered  $\alpha'$ -martensite, plus the d) austenite. A general explanation of the e) state of the multi-phase grain after deformation is also provided.

In this work, the crystal plasticity model is implemented in a Taylor-based finite-strain framework to efficiently capture the most relevant physical parameters in a given phase and simulate the stress-strain response of the multi-phase material. This framework is simulated within the Abaqus software user material subroutine (UMAT) capabilities. The uniaxial tensile specimen was discretized using 30,000 finite-elements to provide a comparison with empirical DIC measurements of the entire tension test, including necking. Each tensile specimen simulation harnessed 32 CPUs and took approximately 6 h to complete.

Each finite-element is a tri-linear hexahedral element with 8 integration points (Figure 1a). At each integration point, 500 multi-phase grains were considered in the context of the Taylor iso-strain local boundary condition approach [52], such that grain morphology and grain interactions are not considered. The iso-strain approach provides a satisfactory homogenized response with known and reasonable over prediction [53] and has been used to model the tensile specimen size-scale for various multiphase alloys [54,55]. As illustrated in Figure 1b, an initial multi-phase grain is simply a coarse-sized recovered  $\alpha'$ -martensite grain that contains an ultrafine austenite grain and an ultrafine ferrite grain. Each of the phases within the multi-phase grain was idealized using a single orientation and grain size. Since there were 500 multi-phase grains per integration point, the orientations, grain sizes, and phase fractions are assigned to match the respective statistical distributions acquired from the EBSD data (Figure 1c/d). Based on the empirical evidence presented later, dislocation density, mechanical twinning, and strain-induced phase

transformations are incorporated into the model (Figure 1e). The constitutive formulae are presented in numerical order, based on the sequence of hierarchy in the general crystal plasticity model.

## 2.5 Microstructure evolution model

In the undeformed microstructure, each multi-phase grain begins with the same initial fraction of UFG austenite ( $f_{\text{ini}}^A = 0.35$ ), UFG ferrite ( $f_{\text{ini},f}^\alpha = 0.10$ ), and coarse-grained recovered  $\alpha'$ -martensite ( $f_{\text{ini},c}^{\alpha'} = 0.55$ ), where the summation of volume fractions of all phases in each multi-phase grain is set to 1.

$$f_{\text{ini}}^{A(k)} + f_{\text{ini},f}^{\alpha(k)} + f_{\text{ini},c}^{\alpha'(k)} = 1$$

Equation 1

The subscript ‘ini’ indicates the initial state; c and f represent grain size (coarse and fine);  $k$  is a counter for each multi-phase grain and  $N$  ( $k = 1, \dots, N$ ) is the number of all multi-phase grains. As deformation takes place (see Figure 1d) the initial fraction of austenite ( $f_{\text{ini}}^A$ ) decomposes into epsilon martensite ( $f^\varepsilon$ ), twinned austenite ( $f^{\text{tw}}$ ), a strain-induced transformation to  $\alpha'$ -martensite ( $f_{\text{sit}}^{\alpha'}$ ), and the remaining austenite ( $f^A$ ) that has only deformed by slip.

$$f_{\text{ini}}^{A(k)} = f^{\varepsilon(k)}(t) + f^{\text{tw}(k)}(t) + f_{\text{sit}}^{\alpha'(k)}(t) + f^A(k)(t) = \text{constant}$$

Equation 2

Substituting Equation 2 into Equation 1 yields Equation 3.

$$f^A(k)(t) + f^{\varepsilon(k)}(t) + f^{\text{tw}(k)}(t) + f_{\text{sit}}^{\alpha'(k)}(t) + f_{\text{ini},c}^{\alpha'(k)} + f_{\text{ini},f}^{\alpha(k)} = 1$$

Equation 3

The initial ferrite and  $\alpha'$ -martensite do not transform since the grains only deform by slip (the volume fraction does not change), whereas the austenite can both slip and transform. In order to obtain physically meaningful material parameters, the volume fraction constraints are applied at the beginning of each time increment. Any variable evolving with time is identified with a  $(t)$  field in the respective equation.

TEM analysis in the present work shows that mechanical twins are observed as early as 8 % engineering strain ( $s = 0.08$ ) and the assumption is that the austenite does not transform before  $s = 0.08$ . EBSD results in the present work show that  $f_{\text{ini}}^A = 0.352$  is reduced to  $f_{\text{min}}^A = 0.182$  in a tensile specimen deformed to failure at the engineering strain of 25 % ( $s = 0.25$ ). The evolution of austenite volume fraction inside multi-phase grain is defined in Equation 4.

$$f^{A(k)}(t) = \begin{cases} f_{\text{ini}}^A = 0.352 & s = 0.08 \\ f_{\text{ini}}^A - f^{\varepsilon(k)}(t) - f^{\text{tw}(k)}(t) - f_{\text{sit}}^{\alpha'(k)}(t) & s \in (0.08, 0.25) \\ f_{\text{min}}^A = 0.182 & s = 0.25 \end{cases}$$

Equation 4

When the austenite fraction in the entire specimen reaches 0.182 transformation is halted. This means that some austenite grains will completely transform, while others will not.

The volume-averaged stress in a given integration point and thus in the  $k^{\text{th}}$  multi-phase grain is detailed in Equation 5.

$$\bar{\sigma}(t) = \sum_{k=1}^N \sigma^{(k)}(t) \frac{|\theta^k|}{|\theta|} \text{ such that:}$$

$$\sigma^{(k)}(t) = \left( f^A(t) + f^{\text{tw}}(t) \right) \sigma^A(t) + \left( f^\varepsilon(t) \right) \sigma^\varepsilon(t) + \left( f_{\text{ini},f}^{(k)} \right) \sigma^{\alpha(k)}(t)$$

$$+ \left( f_{\text{sit}}^{\alpha'(k)}(t) + f_{\text{ini},c}^{\alpha'(k)} \right) \sigma^{\alpha'(k)}(t)$$

Equation 5

The total volume of the representative volume element (RVE) is  $\theta$  and  $\theta^k$  is the volume of the  $k^{\text{th}}$  multi-phase grain.  $\bar{\sigma}$  and  $\sigma^{(k)}$  are the volume average Cauchy stress over the RVE and the  $k^{\text{th}}$  grain.

In what follows (Equations 6-28), the plasticity-enhancing mechanisms were incorporated in every multi-phase grain. For clarity, the  $(k)$  counter and volume average equations are omitted in Equations 6-28. When considering the plasticity-enhancing mechanisms, work by Bouaziz *et al.* [56] described the kinetics of twinning by a phenomenological law where  $\alpha^{\text{tw}} = 3$  and  $m = 2$  are dimensionless parameters extrapolated from the literature,  $f_{\text{max}}^{\text{tw}} = 0.2$  is the saturation fraction of twinning and  $\gamma_{\text{tot}}$  is the total shear strain [45,57,58].

$$f^{\text{tw}}(t) = f^A(t) f_{\text{max}}^{\text{tw}} (1 - \exp(-\alpha^{\text{tw}}(\gamma_{\text{tot}} - \gamma_c)))^m$$

Equation 6

A deformation twin forms ( $f^{\text{tw}}$  increases) when the total shear strain ( $\gamma_{\text{tot}}$ ) is greater than a critical value ( $\gamma_c$ ), otherwise  $f^{\text{tw}} = 0$  (when  $\gamma_{\text{tot}} < \gamma_c$ ). Also,  $\gamma_c$  linearly depends in grain size. Twin fraction increases with strain (after a given strain value) even though the local fraction can decrease near a twin-twin intersection that creates  $\alpha'$ -martensite [9,13,45,59].

There is debate in the literature as to what exact mechanism controls mechanical twinning and the formation of epsilon martensite [60–73]. The assumption used in this constitutive model is that the mechanisms share a relationship through the movement of  $1/6<112>$  type partial dislocations. Therefore, the epsilon martensite kinetics are described by a similar law as compared to the twinning mechanism and shown in Equation 7.

$$f^\varepsilon(t) = f^A(t) f_{\text{max}}^\varepsilon (1 - \exp(-\alpha^\varepsilon(\gamma_{\text{tot}} - \gamma_c)))^m$$

Equation 7

For transformation kinetics from austenite to  $\alpha'$ -martensite through twinning intersections, a modified Olson-Cohen model [74] was employed where  $f_{\text{sit,tw}}^{\alpha'}$  is the volume fraction of strain-induced  $\alpha'$ -martensite from twin intersections [9].

$$f_{\text{sit,tw}}^{\alpha'}(t) = f^A(t) (1 - \exp(-\beta^{\alpha'} f^{\text{tw}}(t)))^n$$

Equation 8

Similar to the work by Lee and De Cooman [75] on a Fe-10Mn-3Al-2Si-0.3C steel, the  $f^A(t)$  term is included in Equation 8 because the austenite in this material does not completely transform. The  $\alpha'$ -martensite evolution in this equation depends on the twinning activity rather than shear-banding [74].  $\beta^{\alpha'}$  is a parameter related to the probability that twin intersections nucleate  $\alpha'$ -martensite. The exponent  $n$  is a fixed term that relates to the number of intersections in the austenite based on the morphology and orientation distribution of the austenite [75][76].

For austenitic steels with a lower SFE [77,78], the strain-induced  $\alpha'$ -martensite usually depends on the volume fraction of  $\varepsilon$ -martensite. The Olson-Cohen model is typically employed for epsilon-epsilon intersections, though other models exist [74,79–87]. Here, the phase transformation from austenite to  $\varepsilon$ -martensite is considered in Equation 9 where  $p^c$  stands for the critical value of the transformation driving force [88].

$$\dot{f}^t(t) = \begin{cases} \dot{f}_{\max}^t \tanh\left(\frac{1}{v} \cdot \frac{p^t - p^c}{p^c}\right) & \text{if } p^t > p^c \\ 0 & \text{otherwise} \end{cases} \quad f_{\text{sit},\varepsilon}^{\alpha'}(t) = \sum_{t=1}^{N_{tr}} f^t$$

Equation 9

$$p^t = b^t \cdot (\mathbf{F}^e \cdot \boldsymbol{\sigma} \cdot \mathbf{F}^e \cdot \boldsymbol{\sigma}) \cdot m^t - \rho_0 \frac{\lambda_T}{\theta_T} (\Theta - \theta_T)$$

Equation 10

In Equation 9,  $\dot{f}_{\max}^t$  is the maximum transformation rate,  $v$  is the viscosity-like parameter and  $p^t$  is the athermal transformation driving force (transformation shear stress). The resulting strain-induced transformation to  $\alpha'$ -martensite from intersection of  $\varepsilon$ -martensite ( $f_{\text{sit},\varepsilon}^{\alpha'}$ ) is counted in Equation 9.  $p^t$  is defined in Equation 10 where  $b^t \cdot m^t$  is the phase transformation system,  $\rho_0$  is mass density,  $\lambda_T$  is the latent heat, and  $\theta_T$  is the transformation temperature.

Table S 1 in the supplementary material provides a description of variables listed in this section, as well the corresponding origin of a given value (experimental, literature, and calibration of the CPFE model).

## 2.6 Deformation model

The total deformation gradient ( $F$ ) decomposes into three components: elastic ( $F^e$ ), plastic ( $F^p$ ) and transformation ( $F^{tr}$ ). Variables listed in the deformation gradient evolve with time. For simplicity, the time dependence ( $t$ ) is omitted in Equations 11-28. The deformation components act as deformation gradients for each multi-phase grain in the computational domain [88].

$$F = \begin{cases} F^e F^p F^{tr}, \text{austenite} \\ F^e F^p, \text{ferrite and } \alpha' - \text{martensite} \end{cases}$$

Equation 11

Ferrite and recovered  $\alpha'$ -martensite phases do not include a transformation gradient term, so the transformation term is reserved for only austenite grains where  $f^t$  is the volume fraction of phase transformation in the  $t^{\text{th}}$  transformation system [89].

$$F^{\text{tr}} = I + \sum_{t=1}^{N_{\text{trans}}} f^t b_{\text{trans}}^t \otimes m_{\text{trans}}^t = I + \sum_{t=1}^{N_{\text{trans}}} f^t P_{\text{trans}}^t$$

Equation 12

$N_{\text{trans}}$  is the number of phase transformation systems from austenite to  $\varepsilon$ -martensite.  $b_{\text{trans}}^t$  is the average transformation direction and  $m_{\text{trans}}^t$  is the habit plane normal [90].  $P_{\text{trans}}^t$  is the Schmid tensor for the  $t^{\text{th}}$  transformation system.  $I$  represents the two-dimensional identity matrix.

The elastic constitutive relationship is defined in Equation 13 where the Green strain ( $E^e$ ) and the 2nd Piola-Kirchhoff stress ( $T^e$ ) are respectively defined in Equation 14 and Equation 15 [91].

$$T^e = C : E^e$$

Equation 13

$$E^e = \frac{1}{2}(F^{eT} \cdot F^e - I)$$

Equation 14

$$T^e = F^{e-1} [\det(F^e) \cdot \sigma] F^{e-T}$$

Equation 15

The material derivative of plastic deformation gradient ( $F^p$ ) results in the plastic velocity gradient  $L^p$  [88].

$$L^p = \dot{F}^p \cdot F^{p-1} = \begin{cases} f^A \sum_{\alpha=1}^{N_{\text{slip}}} \dot{\gamma}^\alpha P_{\text{slip}}^\alpha + f^{\text{tw}} \sum_{\beta=1}^{N_{\text{twin}}} \dot{\gamma}^\beta P_{\text{twin}}^\beta, & \text{austenite} \\ f^M \sum_{\alpha=1}^{N_{\text{slip}}} \dot{\gamma}^\alpha P_{\text{slip}}^\alpha, & \text{ferrite and } \alpha' - \text{martensite} \end{cases}$$

Equation 16

Dislocation slip and twinning are both considered in the austenite phase, whereas for the ferrite and martensite phases,  $F^p$  is described only by dislocation slip.  $N_{\text{slip}}$  and  $N_{\text{twin}}$  are the number of slip and twin systems, respectively.  $\dot{\gamma}^\alpha (\alpha \in [1, N_{\text{slip}}])$  and  $\dot{\gamma}^\beta (\beta \in [1, N_{\text{twin}}])$  are the shear strain rate on slip and twin systems, respectively.  $P_{\text{slip}}^\alpha$  and  $P_{\text{twin}}^\beta$  are the Schmid tensors for the dislocation slip and twin systems, such that the unidirectional nature of twinning [92] was considered in the model [68,93].  $f^A$  is the volume fraction of austenite and  $f^M$  is the volume fractions of ferrite and  $\alpha'$ -martensite phases.

Thermal activation is included in the model to consider the effect of strain rate. The shear strain rate of dislocation slip, or twinning is affected by the SFE. In this study, the thermally activated shear strain is defined in Equation 17 where  $\Delta F$  is the Helmholtz free energy, or the

effective activation energy barrier for dislocation glide,  $\rho_m$  is the average mobile dislocation density,  $v_{id}$  is the dislocation vibration frequency,  $b$  is the magnitude of the Burgers vector,  $k_B$  is the Boltzmann constant,  $\vartheta$  is temperature and  $\Delta V$  is the thermal activation volume [94,95]. At high strain rates, heat diffusion is typically slower than the rate of heat generated due to plastic dissipative heating, leading to a local rise in temperature. In such cases, adiabatic assumption is typically used and a fraction of plastic work is converted to heat using the Taylor-Quinney coefficient, which remains local at a material point [96]. However, this coefficient also depends on stress state [97] and is typically used to describe steels containing austenite that readily transforms to martensite [98]. As to be discussed in Section 3.2, the average temperature rise in the current study is moderate until the initiation of necking in the tensile specimen, after which the specimen fails quickly. Hence the dissipative heating is taken to have a relatively small effect on the material behavior in the majority of the loading history and is neglected in the simulations. In regard to the model, it should be noted that the slip rate  $\dot{\gamma}^\alpha$  in the  $\alpha^{\text{th}}$  slip system is activated when the resolved shear stress (RSS)  $\tau^\alpha$  is higher than its critical value  $s^\alpha$  (dislocation resistance or critical resolved shear stress), otherwise  $\dot{\gamma}^\alpha = 0$ .

$$\dot{\gamma}^\alpha = \frac{\rho_m v_{id} b^\alpha}{2} \exp\left(\frac{-\Delta F}{k_B \vartheta}\right) \exp\left(\frac{(\tau^\alpha - s^\alpha)\Delta V}{k_B \vartheta}\right) \operatorname{sgn}(\tau^\alpha)$$

Equation 17

A similar formula describes the mechanism of mechanical twinning in Equation 18 where,  $\tau^\beta$  and  $s^\beta$  represent the resolved shear stress and the twin resistance on the  $\beta^{\text{th}}$  twin system, respectively.

$$\dot{\gamma}^\beta = \begin{cases} \frac{\rho_m v_{id} b^\beta}{2} \exp\left(\frac{-\Delta F}{k_B \vartheta}\right) \exp\left(\frac{(\tau^\beta - s^\beta)\Delta V}{k_B \vartheta}\right) & \text{if } \tau^\beta > s^\beta \\ 0 & \text{otherwise} \end{cases}$$

Equation 18

The critical twinning stress is known to be significantly influenced by grain size for grains smaller than  $0.5 \mu\text{m}$  [61]. The stress constraints indicate that the twinning deformation is directional. The sum of the twinned volumes does not exceed the grain volume, and the twinned region must stay as such unless a transformation occurs.

The shear resistance is decomposed into four terms including the initial temperature associated  $s_0^\alpha$ , Hall-Petch-associated  $s_{\text{HP}}^\alpha$ , forest dislocation density related  $s_{\text{for}}^\alpha$  and debris dislocation density related  $s_{\text{deb}}^\alpha$  [99].

$$s^\alpha = s_0^\alpha + s_{\text{HP}}^\alpha + s_{\text{for}}^\alpha + s_{\text{deb}}^\alpha$$

Equation 19

$$s_{\text{HP}}^\alpha = \mu \text{HP}^\alpha \sqrt{\frac{b^\alpha}{d_g^\alpha}}$$

Equation 20

$$s_{\text{for}}^\alpha = b^\alpha \chi \mu \sqrt{\rho_{\text{for}}^\alpha}$$

Equation 21

$$s_{\text{deb}}^{\alpha} = k_{\text{deb}} \mu b^{\alpha} \sqrt{\rho_{\text{deb}}} \ln \left( \frac{1}{b^{\alpha} \sqrt{\rho_{\text{deb}}}} \right)$$

Equation 22

Here  $\chi$  is the dislocation interaction constant, taken to be 0.31 for Fe-Mn-C steel. The elastic shear modulus ( $\mu$ ) evolves linearly with temperature.  $\rho_{\text{for}}^{\alpha}$  represents the forest dislocation density in a single grain. Here only the self-hardening is considered and the latent hardening is neglected. Stage IV hardening is represented by substructure hardening ( $s_{\text{deb}}^{\alpha}$ ) and  $k_{\text{deb}}$  is a material-independent constant set to 0.1 for both face-centered cubic (FCC) and body-centered cubic (BCC) crystal structures and as 0.086 for hexagonal close-packed (HCP) crystals [100], and finally  $\rho_{\text{deb}}$  is the total debris dislocation density for one grain.  $HP^{\alpha}$  is the Hall-Petch-associated coefficient and  $d_g^{\alpha}$  is the grain size of each corresponding phase.

The twinning propagation resistance  $s_{\text{tw}}^{\beta}$  for  $\beta$ th twin system consists of two components [99] as shown in Equation 23 and Equation 24.

$$s_{\text{tw}}^{\beta} = s_0^{\beta} + s_{\text{HP}}^{\beta}$$

Equation 23

$$s_{\text{HP}}^{\beta} = \mu HP^{\beta} \sqrt{\frac{b^{\beta}}{d_{\text{MTF}}^{\beta}}}$$

Equation 24

The effect of dislocation slip on twinning is already considered in the volume fraction evolution (see Equation 6) and the plastic deformation gradient (see Equation 16), so the interaction between mechanical twins and forest dislocations is neglected [99].  $s_0^{\beta}$  is the initial propagation resistance and  $s_{\text{HP}}^{\beta}$  is the Hall-Petch-like strength related to the twin boundaries.  $d_{\text{MTF}}^{\beta}$  denotes the width of the mean free dislocation path, which is approximated as the grain size of newly transformed  $\alpha'$ -martensite. The forest dislocation density evolution is related to the storage rate and recovery rate in the form of a Kocks-Mecking ansatz [99].

The evolution of forest dislocation density is shown in Equation 25 and Equation 26.

$$\frac{\partial \rho_{\text{for}}^{\alpha}}{\partial \gamma^{\alpha}} = \frac{\partial \rho_{\text{gen}}^{\alpha}}{\partial \gamma^{\alpha}} - \frac{\partial \rho_{\text{rec}}^{\alpha}}{\partial \gamma^{\alpha}} = k_1 \sqrt{\rho_{\text{for}}^{\alpha}} - k_2(\dot{\gamma}, \vartheta) \rho_{\text{for}}^{\alpha}$$

Equation 25

$$k_2(\dot{\gamma}, \vartheta) = k_1 \frac{b^{\alpha} \chi}{g^{\alpha}} \left[ 1 - \frac{k \vartheta}{\widehat{D} b^3} \ln \left( \frac{\dot{\gamma}}{\dot{\gamma}_0} \right) \right]$$

Equation 26

$k_1$  is an adjustable coefficient related to the generation of statistically stored dislocations due to forest trapping of mobile dislocations and  $k_2$  is the rate-sensitive coefficient for dynamic recovery.  $g^{\alpha}$  is the normalized stress-independent activation energy,  $\dot{\gamma}_0$  is the reference strain rate, and  $\widehat{D}$  is

the drag-stress [99,101].

The debris dislocation density evolution ( $\Delta\rho_{\text{deb}}$ ) is defined as the sum of effects from multiple slip systems for one grain where  $q^\alpha$  is a rate coefficient [99] related to the thermal-activated energy and volume, describing how point defects can grow into debris by local thermal activation.

$$\Delta\rho_{\text{deb}} = \sum_\alpha \frac{\partial\rho_{\text{deb}}}{\partial\gamma^\alpha} d\gamma^\alpha = \sum_\alpha q^\alpha b^\alpha \sqrt{\rho_{\text{deb}}} k_2^\alpha(\dot{\gamma}^\alpha, \vartheta) \rho_{\text{for}}^\alpha$$

Equation 27

Table S 2 in the supplementary material provides a description of variables listed in this section, as well the corresponding origin of a given value (experimental, literature, and calibration of the CPFE model).

### 3. Results

#### 3.1 Characterization of the as-received material

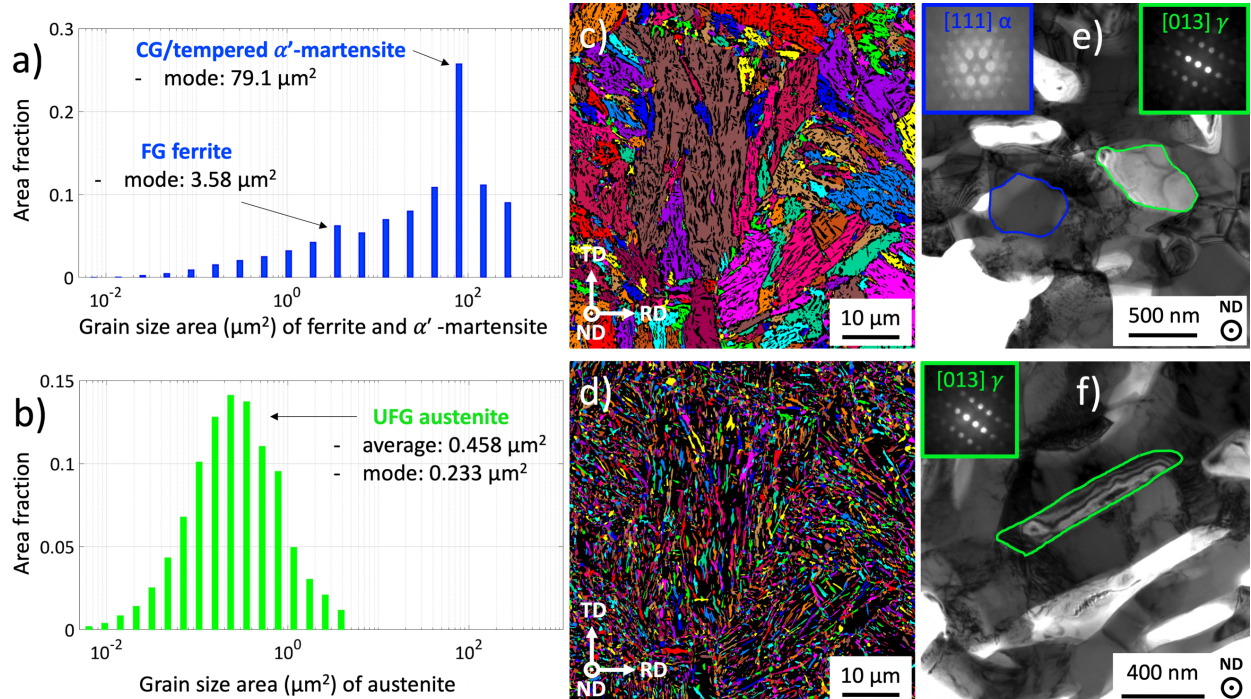


Figure 2: Grain size area distributions measured with EBSD (x-axis plotted in log scale), separated by phase with corresponding unique-grain maps (color has no quantitative meaning, but rather designates the location of an individual grain) for a/c)  $\alpha'$ -martensite and FG ferrite, plus b/d) UFG austenite. CG = coarse-grained, FG = fine-grained, and UFG = ultrafine-grained. Area fraction is relative to the area encompassed by each phase of Fe identified with EBSD (i.e. total cumulative area fraction of all austenite grains sums to 1). 200 kV CBED patterns identify e) equiaxed ferrite ( $\alpha$ ) and austenite ( $\gamma$ ) grains, as well as f) elongated rod-like or plate-like austenite grains, as shown in the BF-TEM images.

EBSM and TEM were used to differentiate between the microstructural constituents. Figure 2a-d shows binned diagrams for plotting purposes, but all raw data from EBSD is used in the CPFE

model. Figure 2 shows grain size area, rather than grain size diameter, because diameter is a better representation of equiaxed grains, but not for rod-like or plate-like grains. After intercritical annealing, a sharp peak in Figure 2a indicates a grain size area of  $79 \mu\text{m}^2$  (recovered  $\alpha'$ -martensite), but a smaller peak at  $3.6 \mu\text{m}^2$  reveals the presence of FG ferrite, (consistent with the grain structure observed in Figure 2c). The average austenite grain size area was  $0.46 \mu\text{m}^2$  (Figure 2b) and the percentage of UFG austenite in the multi-phase steel was 35 %. Convergent beam electron diffraction (CBED) analysis (Figure 2e), confirmed the presence of equiaxed UFG ferrite in close proximity to equiaxed UFG austenite. CBED also confirmed a rod-shaped austenite grain (Figure 2f), which is consistent with EBSD measurements (Figure 2d).

### 3.2 Mechanical properties and non-contact thermal measurements

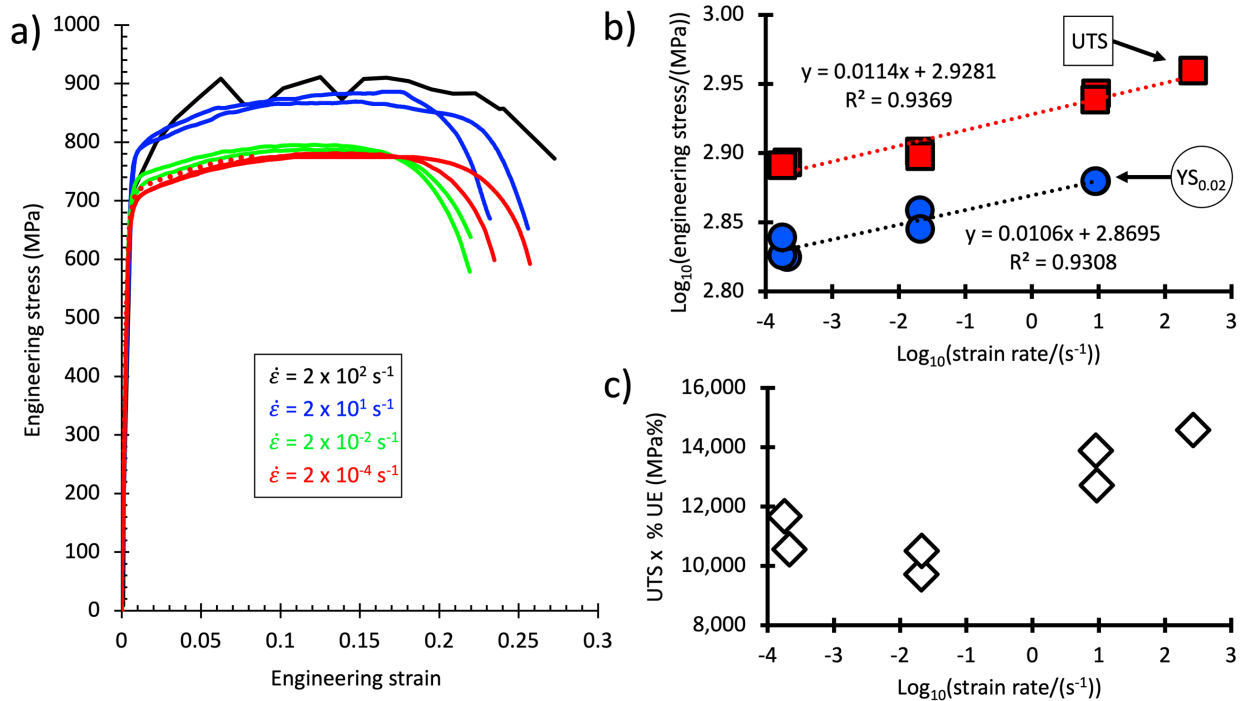


Figure 3: a) Engineering stress-strain curves. Servo-hydraulic tensile tests were performed at nominal strain rates from  $\dot{\epsilon} = 2 \times 10^{-4} \text{ s}^{-1}$  to  $\dot{\epsilon} = 2 \times 10^2 \text{ s}^{-1}$ . An interrupted test deformed at  $\dot{\epsilon} = 2 \times 10^{-4} \text{ s}^{-1}$  is shown as a dotted line. b) Ultimate tensile strength (UTS) and 0.2% offset yield strength (YS) values are shown as a function of strain rate (log scale used to measure strain rate sensitivity). c) The product of UTS and % uniform elongation (% UE) are shown as a function of strain rate.

Figure 3a shows all engineering stress-strain curves measured. The Young's modulus measured during quasi-static strain rates was 180 GPa. Nominal intended strain rates and strain rate sensitivities of relevant tensile properties are shown in Figure 3a-c, which use the actual achieved engineering strain rates. Equation 28 describes the calculation of strain rate sensitivity ( $m$ ) [102]. The strain-rate sensitivities of both the YS and ultimate tensile strength (UTS) are respectively  $m = 0.0106$  and  $m = 0.0114$  for the range of strain rates investigated (Figure 3b). The 0.2% offset yield strength (YS) of the  $\dot{\epsilon} = 2 \times 10^2 \text{ s}^{-1}$  test was not computed because quite few data points make up the stress-strain curve.

$$m = \left( \frac{\partial \log(\sigma)}{\partial \log(\dot{\epsilon})} \right)_{\varepsilon}$$

Equation 28

The product of UTS and % UE decreased slightly from  $\dot{\epsilon} = 2 \times 10^{-4} \text{ s}^{-1}$  to  $\dot{\epsilon} = 2 \times 10^{-2} \text{ s}^{-1}$  (Figure 3c) due to a slight reduction in UE and minimal increase in UTS (Figure 3a), then continually increased through strain rates up to  $\dot{\epsilon} = 2 \times 10^2 \text{ s}^{-1}$ .

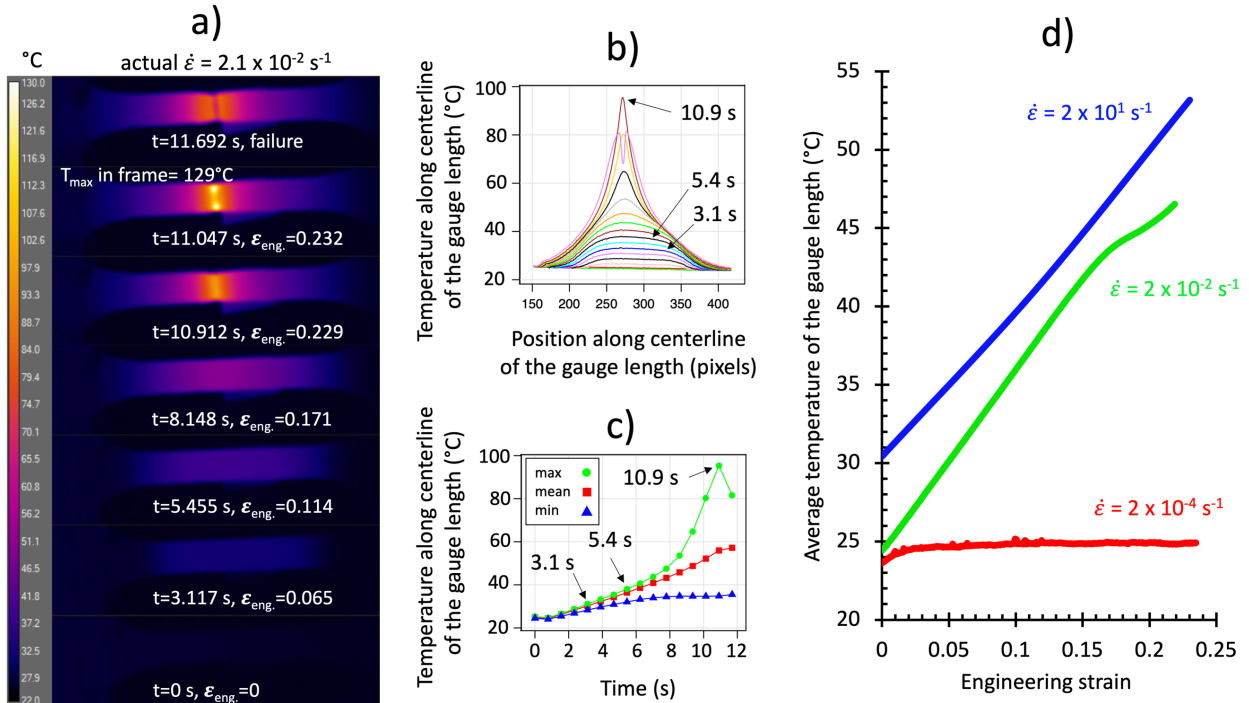


Figure 4: a) Thermal images captured during a tensile test at  $\dot{\epsilon} = 2 \times 10^{-2} \text{ s}^{-1}$ . b) Non-contact temperature measurements using a line drawn across the centerline of the gauge length are shown as profile plots for various time steps. c) The maximum, mean, and minimum temperatures across the centerline of the gauge length are plotted as functions of time for the test at  $\dot{\epsilon} = 2 \times 10^{-2} \text{ s}^{-1}$ . d) Average surface temperatures of areas in the reduced section of the gauge length are measured at various strain rates.

Thermal images of a specimen deformed at  $\dot{\epsilon} = 2 \times 10^{-2} \text{ s}^{-1}$  (Figure 4a) show that localized deformation does not occur until after UTS (at 0.171 engineering strain). Up until the point of necking, the dissipative heating was moderate since the average temperature of the gauge length increased by only 20 °C (see Figure 4d). Localized heat was generated at the center of the gauge length at 0.229 engineering strain (see Figure 4a), near the eventual necked region. No evidence of Lüders bands or PLC bands were observed in any of the tension tests. The large temperature rise (Figure 4b-c) remained local to the necked region and the specimen failed quickly thereafter. The fracture surface of the specimen deformed at  $\dot{\epsilon} = 2 \times 10^{-2} \text{ s}^{-1}$  (Figure 4a) showed extensive evidence of ductile failure from micro-void coalescence. Ductile failure by micro-void coalescence was also observed for samples deformed at strain rates from  $\dot{\epsilon} = 2 \times 10^{-4} \text{ s}^{-1}$  to  $\dot{\epsilon} = 2 \times 10^1 \text{ s}^{-1}$ . Just before fracture, the area of the necked region has a higher temperature (max temperature of 129

°C), indicating that more strain has been accommodated in the neck, which is consistent with strain-mapping (DIC results shown later).

The ResearchIR™ software was used to record the average surface temperature across the entire area of the reduced gauge length, excluding the necked region and fracture surface. Representative temperature plots as a function of engineering strain for strain rates from  $\dot{\epsilon} = 2 \times 10^{-4}$  s<sup>-1</sup> to  $\dot{\epsilon} = 2 \times 10^1$  s<sup>-1</sup> are shown in Figure 4d. The average temperature in Figure 4c (average temperature across the centerline just before fracture is 58 °C) is higher than the average temperature of the reduced gauge length before fracture (48 °C), even though these data are from the same test. Clearly, incorporating the temperature of the necked region in the computation increases the average temperature and thus accounts for the 10 °C temperature difference. In the case of the  $\dot{\epsilon} = 2 \times 10^1$  s<sup>-1</sup> tests, the initial tensile-specimen temperature was higher because of the high intensity of the halogen lights (necessary for illumination during DIC measurements), which were turned on 30 s before the test. Nevertheless, the final average temperature in the area of the reduced gauge length after deformation at  $\dot{\epsilon} = 2 \times 10^1$  s<sup>-1</sup> is only 30 °C greater than at the quasi-static strain rates.

### 3.3 Deformation mechanisms

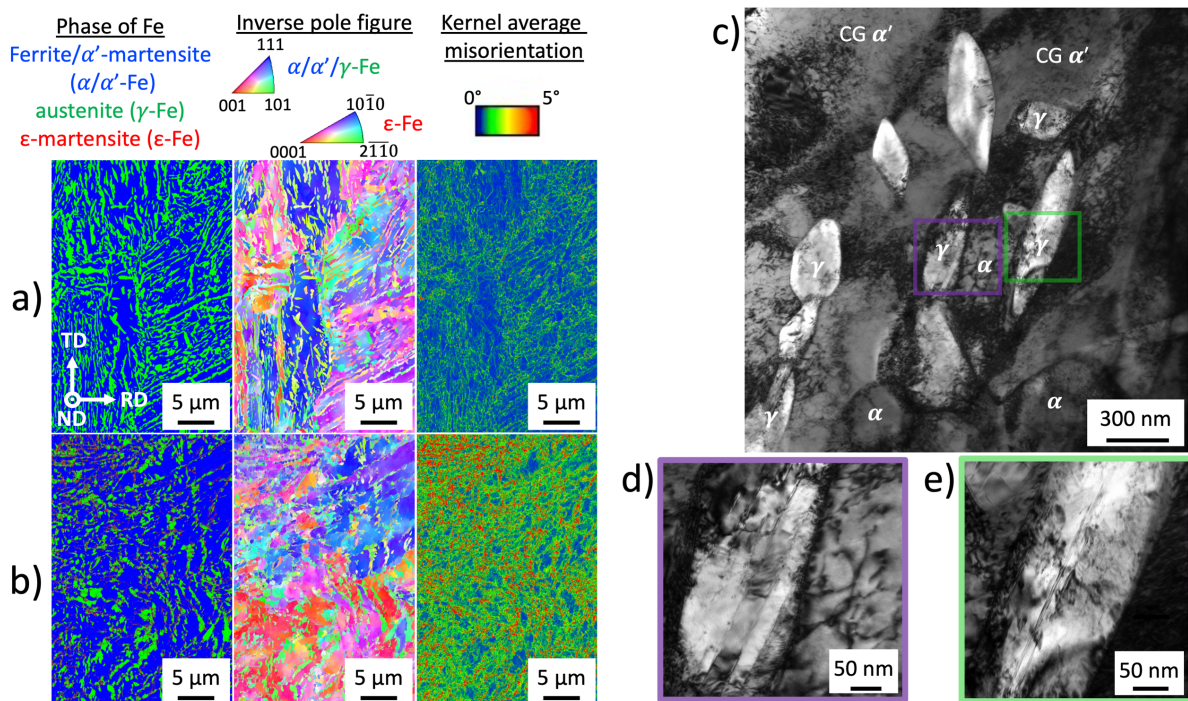


Figure 5: EBSD comparison of a) as-received specimen and b) specimen deformed to failure at quasi-static strain rates. c-e) BF-TEM images of deformation accommodated by the coarse-grained recovered (CG)  $\alpha'$ -martensite, UFG ferrite ( $\alpha$ ), and UFG austenite ( $\gamma$ ).

A key characteristic of hot- and/or cold-rolled medium-Mn steels is the UFG microstructure produced during intercritical annealing. Through a Hall-Petch relationship, the ultrafine grain size is one of the main contributors to the high YS. EBSD results of the as-received and deformed microstructures (Figure 5) indicate that the austenite volume fraction decreased (from 35 to 18 %) after deformation to failure at quasi-static strain rates and also revealed a small

volume fraction of  $\varepsilon$ -martensite (4 %) within the austenite grains. A comparison between as-received and pulled-to-failure microstructures (Figure 5a-b) showed an increase in the average Kernel average misorientation (KAM) (a 67 % increase in austenite and a 77 % increase in ferrite/recovered  $\alpha'$ -martensite). The martensitic matrix, ultrafine ferrite, and ultrafine austenite in the deformed material (Figure 5c-e) respectively contain dislocation tangles and planar defects that were not present in the undeformed material (Figure 2e-f). Much of the austenite remained untransformed after deformation to failure (consistent with EBSD results).

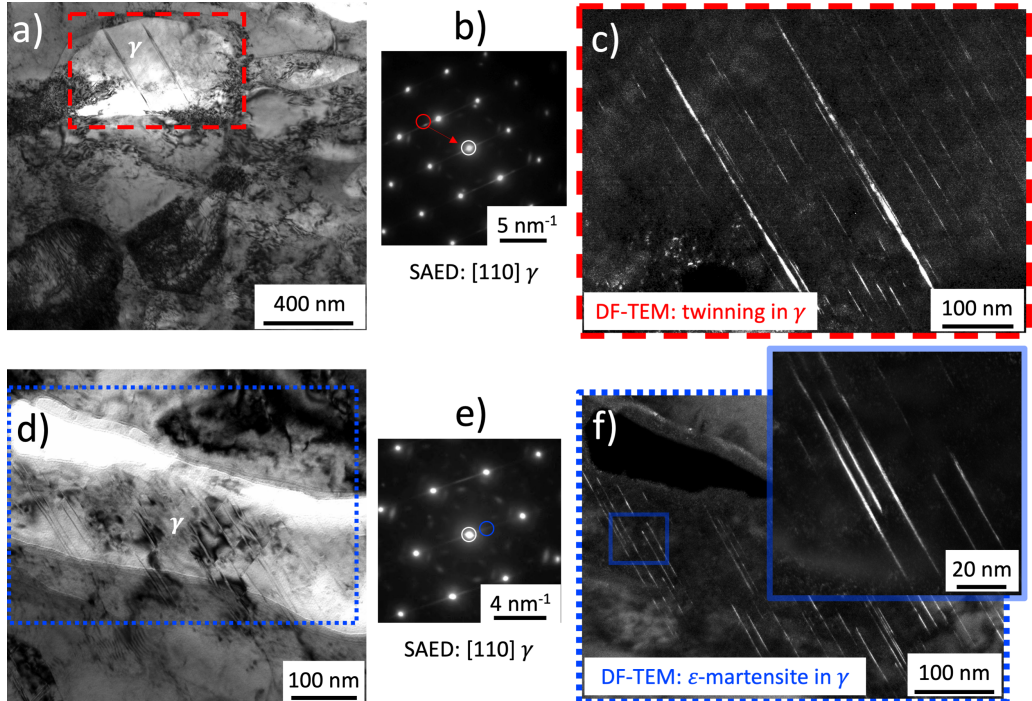


Figure 6: a/d) BF-TEM and c/f) DF-TEM images of planar defects visible in austenite grains from specimens deformed to failure at  $\dot{\varepsilon} = 2 \times 10^{-4} \text{ s}^{-1}$ . b/e) Selected area electron diffraction results indicate two types of planar defects present in the ultrafine-grained austenite that has not completely transformed: mechanical twinning and hexagonal  $\varepsilon$ -martensite.

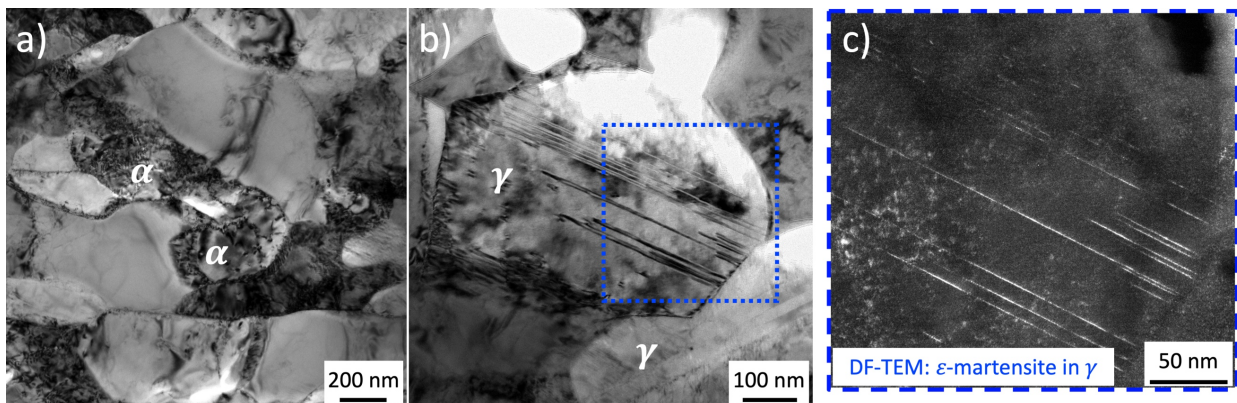


Figure 7: BF-TEM images of a sample interrupted at  $\varepsilon_{\text{eng.}} = 0.08$  (tested at  $\dot{\varepsilon} = 2 \times 10^{-4} \text{ s}^{-1}$ ). a) UF ferrite grains shows signs of deformation with dislocation tangles and b) UF austenite grains have already begun to develop planar defects (stacking faults and  $\varepsilon$ -martensite).

Dark-field TEM results from samples deformed to failure at  $\dot{\varepsilon} = 2 \times 10^{-4} \text{ s}^{-1}$  (Figure 6) and  $\dot{\varepsilon} = 2 \times 10^1 \text{ s}^{-1}$  confirm the presence of mechanical twins and hexagonal  $\varepsilon$ -martensite in the ultrafine austenite grains that have not completely transformed (consistent with SFE predictions). In Figure 7b-c, BF-TEM and DF-TEM images show strain-induced planar defects in the austenite of a sample deformed at  $\dot{\varepsilon} = 2 \times 10^{-4} \text{ s}^{-1}$  and interrupted at  $\varepsilon_{eng.} = 0.08$ . Figure 7a provides evidence that UF ferrite grains have also begun to deform.

### 3.4 Model calibration

Table 2: Elastic properties from [72,103] used in the appropriate constitutive equations

Phase	C <sub>11</sub> (GPa)	C <sub>12</sub> (GPa)	C <sub>44</sub> (GPa)	C <sub>13</sub> (GPa)	C <sub>33</sub> (GPa)
Austenite ( $\gamma$ )	174	85	99		
Martensite ( $\alpha'$ )	169	82	96		
Ferrite ( $\alpha$ )	175	82	97		
Martensite ( $\varepsilon$ )	420	30	320	120	570

Table 3: Parameters most sensitive to the calibration process and used to determine plastic properties from tensile data at various strain rates.

Parameters	BCC( $\alpha, \alpha'$ )	HCP ( $\varepsilon$ )	FCC ( $\gamma$ )
$\Delta F$ (J)	$4.45 \times 10^{-20}$	$5.36 \times 10^{-20}$	$6.39 \times 10^{-21}$
$\Delta V^\alpha$ (m <sup>3</sup> )	$7.68 \times 10^{-29}$	$4.19 \times 10^{-29}$	$6.25 \times 10^{-28}$
$b^\alpha$ (μm)	$2.50 \times 10^{-4}$	$2.48 \times 10^{-4}$	$2.56 \times 10^{-4}$
$s_0^\alpha$ (MPa)	247	550	168
$s_0^\beta$ (MPa)	N/A	N/A	209
$HP^{\alpha\beta}$ (MPa)	130	120	134
$k_1$ (m <sup>-1</sup> )	$4.29 \times 10^7$	$1.08 \times 10^{10}$	$3.51 \times 10^8$
$g^\alpha$	$1.21 \times 10^{-2}$	$3.44 \times 10^{-2}$	$4.52 \times 10^{-2}$

Anisotropic elastic properties used in the CPFE model are shown in Table 2, while relative orientations of the as-received microstructure are based on EBSD measurements. Calibration of the physical parameters in the CPFE model was completed by minimizing the difference between the experimental stress-strain data sets and the stress-strain data generated by the CPFE model. The optimization was deemed completed when the average error between experimental and model data points was less than 3%. The most sensitive plastic variables that provided the greatest influence on the optimization of experimental and model data for all strain rates are shown in Table 3.

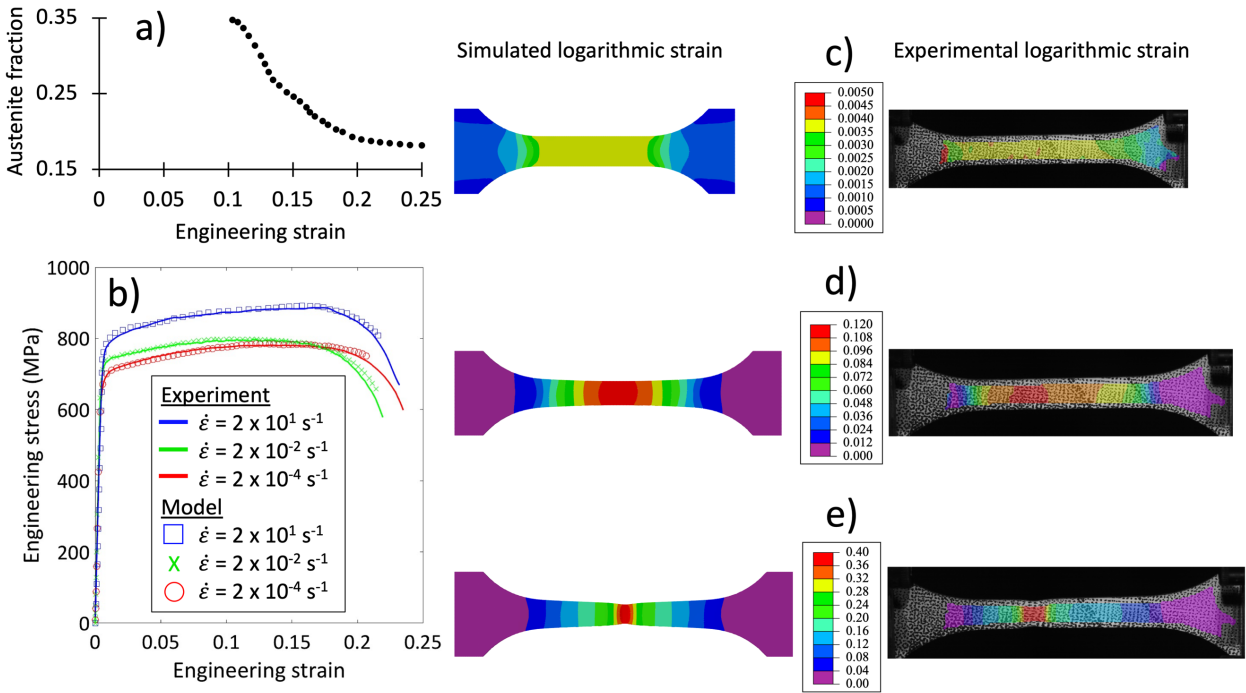


Figure 8: a) Evolution of austenite volume fraction as a function of engineering strain constrained by EBSD results from the as-received and pulled-to-failure microstructures. b) Resulting tensile properties from the CPFE model are compared to the experimental results (strain rates from  $\dot{\epsilon} = 2 \times 10^{-4} \text{ s}^{-1}$  to  $\dot{\epsilon} = 2 \times 10^1 \text{ s}^{-1}$ ). c-e) CPFE-based logarithmic strain and DIC logarithmic strain are compared for a test deformed at  $\dot{\epsilon} = 2 \times 10^{-4} \text{ s}^{-1}$ .

Figure 8a shows the evolution of the austenite volume fraction. A comparison of the calibrated CPFE simulation and experimental mechanical properties (Figure 8b) is provided for samples deformed at nominal strain rates of  $\dot{\epsilon} = 2 \times 10^{-4} \text{ s}^{-1}$ ,  $\dot{\epsilon} = 2 \times 10^{-2} \text{ s}^{-1}$ , and  $\dot{\epsilon} = 2 \times 10^1 \text{ s}^{-1}$ . The strain-rate sensitivity of this material was captured in the thermal activation volume and thermal activation energy barrier of FCC and BCC crystals. Consequently, one single set of physical parameters was identified to capture the mechanical behavior at different strain rates. Results in Table 3 show that the thermal activation energy barrier ( $\Delta F$  in Joules) is higher for BCC than for FCC. Calibration results were consistent with the prediction that short-range barriers in BCC (Peierls barriers) play a larger role in the positive strain rate sensitivity of yield strength as the majority of the microstructure is BCC-based. The effectiveness of forest dislocations on inhibiting mobile dislocation motion in FCC is greater than BCC in this study (see  $k_1$  in Table 3) and indicates the UFG austenite may also contribute to the positive strain rate sensitivity of this material.

Figure 8c-e provides DIC images for a tensile specimen deformed at  $\dot{\epsilon} = 2 \times 10^{-4} \text{ s}^{-1}$ , plus a comparison of logarithmic strain generated with the Taylor model is shown side-by-side with identical scales of logarithmic strain. The CPFE-based logarithmic strain images show necking in the middle of the tensile bar (due to boundary-condition imposed constraints). However, the experimental DIC images show necking occurring slightly off center (due to the natural effect of microstructural variation along the gauge length). Good agreement is noted between the experimental DIC images and CPFE-based logarithmic strain images in terms of the magnitude and gradient of logarithmic strain, but an exact match is generally not possible since the entire tensile bar was not completely characterized.

## 4. Discussion

### 4.1 Influences of microstructural constituents on plastic instabilities of multi-phase steel

The unique microstructure of the current multi-phase material contains recovered  $\alpha'$ -martensite, UFG ferrite, and 35 % UFG austenite with multiple morphologies (equiaxed, rod-like and plate-like). This cold-rolled and annealed medium-Mn does not contain colonies of lamellar UFG austenite, but rather a mix of morphologies and relatively random crystallographic orientations (no fiber textures or complete colonies of lamellar austenite), consistent with previous work on similar steel compositions [49,104,105]. The mixed morphology of the multi-phase microstructure may wash out effects from grain morphology in the context of the entire tensile bar since there is a relatively equal likelihood of observing equiaxed and non-equiaxed austenite grains. Recent work [106] completed on a similar steel shows how hot rolled and cold rolled steels can both exhibit continuous yielding, but the differences in grain morphology, spatial alignment of grains and crystallographic orientation of UFG austenite influence the yielding and strain hardening behavior.

Lüders bands and PLC bands are not observed in the current work. The absence of discontinuous yielding (Lüders banding) is attributed to the recovery of the cold-rolled martensite (rather than a complete recrystallization), the morphology of the recovered microstructure, plus the relatively small grain size and volume fraction of the UFG ferrite [10,39,49,107–112]. Further, the annealing temperature in the current work is well below the predicted  $T_{\gamma-\max}$ , meaning that the austenite is relatively mechanically stable and does not transform to athermal martensite during quenching from the intercritical annealing step [48,111]. The absence of PLC bands has been attributed by others [30,31,33] to both the morphology of all micro-constituents and the ultra-low carbon content. Work on a similar steel composition by Haupt *et al.* [104] showed no evidence of Lüders band formation (described as discontinuous yielding and manifested by heterogeneous deformation) and no evidence of PLC bands (serrations in the stress-strain curve) during tensile deformation with samples annealed at 555 °C for 1 h, 5 h and 15 h. by Ma *et al.* [49] observed a similar microstructure and mechanical response for the 555 °C annealing temperature, but then measured discontinuous yielding and observed an equiaxed microstructure in samples annealed at 600 °C and 650 °C.

### 4.2 Influences of strain rate on the mechanical properties of multi-phase steel

The strain-rate sensitivities of the yield and ultimate tensile strengths are positive, which indicates that thermally activated and time-dependent short-range barriers dominate the flow stress [102,113,114]. For BCC metals, the primary short-range dislocation barrier is the frictional-based Peierls-Nabarro stress, while for FCC metals, the primary short-range dislocation barriers are dislocation forests and solute atoms [76,115]. Notably, when only crystal structure is considered, the Peierls barrier (in energy per unit length [116]) is more difficult to overcome in the BCC lattice as compared to short-range barriers in the FCC lattice [113]. This indicates that the predominant strain-rate sensitivity effect on flow stress in this material is related to the ferritic and martensitic microstructural constituents, which is especially true since the initial austenite content is only 35 %.

No change in dominating deformation mechanism is assumed for the investigated range of strain rates. This assumption is used in the CPFE model because DF-TEM observations

indicate that both mechanical twinning and  $\varepsilon$ -martensite are active in samples deformed to failure at  $\dot{\varepsilon} = 2 \times 10^{-4} \text{ s}^{-1}$  through  $\dot{\varepsilon} = 2 \times 10^1 \text{ s}^{-1}$ . To obtain more details along this line, further investigation of the microstructure evolution at high strain rates would require interrupted tests [117] and would allow for a more concrete comparison of microstructure effects on UTS as well as initiation of twinning and transformation.

Measuring temperature evolution provides insight into operable deformation mechanisms. The average temperature measured in the gauge length indicates that the specimen heating falls somewhat short of what is predicted for adiabatic heating conditions at  $\dot{\varepsilon} = 2 \times 10^{-2} \text{ s}^{-1}$ . Under adiabatic heating conditions, the temperature generated is proportional to the total plastic work [69,118]. The expected temperature rise under completely adiabatic conditions was calculated using an accepted formula [61,72,118] for estimating temperature rise during measured plastic work. Relevant parameters include a 90 % efficiency in conversion of mechanical energy to heat energy, a heat capacity of 0.46 kJ/(kg K), and a mass density of 7.4 g/cm<sup>3</sup>. As expected, quasi-static strain rates ( $\dot{\varepsilon} = 2 \times 10^{-4} \text{ s}^{-1}$ ) showed no signs of tensile specimen heating (except after fracture). The predicted rise in specimen temperature for a  $\dot{\varepsilon} = 2 \times 10^{-2} \text{ s}^{-1}$  test is  $\Delta T = 40 \text{ }^\circ\text{C}$  and for the  $\dot{\varepsilon} = 2 \times 10^1 \text{ s}^{-1}$  test is  $\Delta T = 48 \text{ }^\circ\text{C}$  (based on adiabatic conditions and the numerically integrated engineering stress-strain curve). Given the comparison with these predicted temperature rises and results in Figure 4d, the heating conditions are still short of adiabatic by 15 °C. Thus, it is likely that adiabatic conditions may actually be satisfied at  $\dot{\varepsilon} = 2 \times 10^{-2} \text{ s}^{-1}$ . Further, thermodynamic calculations [25] show that an increase in temperature from 24 °C to 54 °C ( $\Delta T = 30 \text{ }^\circ\text{C}$ ) should not raise the SFE of the austenite by more than 4 mJ/m<sup>2</sup>. The pioneering work by Frommeyer *et al.* [119] shows that in coarse-grained austenitic steels, adiabatic heating generated from high-rate deformation stabilizes austenite and raises the SFE, which increased the strain hardening rate and uniform elongation in TRIP steels, and decreased the twinning rate and drawability of TWIP steels. Similar observations were made on the role of dissipative heating on the interplay of twinning and dislocation activity in another coarse-grained steel (alloyed with a mass fraction of 3 % Si) [120]. Given the large ductility (80% elongation) in those steels [119], the role of adiabatic heating plays a key role. However, most third generation AHSS do not elongate nearly as much as second generation AHSS. Thus, the influence of strain rate is more complex for third generation AHSS since austenite is not the major microstructural constituent by volume and the austenite is ultrafine in size.

The medium-Mn steel in this work does not show evidence of PLC bands, the uniform and total elongations (UE and TE) do not exhibit strain rate sensitivity, the UTS has a positive strain rate sensitivity, and similar deformation mechanisms are observed at low and high strain rates. Based on this evidence, it is assumed that the specimen heating does not strongly influence the deformation mechanisms in this specific multi-phase steel. However, the UTS strain rate sensitivity of other UFG medium-Mn TRIP steels [76,121–123] is negative. In those cases [76,121–123] the austenite completely transforms to  $\alpha'$ -martensite at quasi-static strain rates before failure. The austenite to martensite transformation rate in advanced high-strength sheet steel can be reduced [76] at high strain rates if the transformation occurs at large levels of strain because the heat builds up in the tensile specimen and stabilizes the austenite by increasing the SFE. In the case of the 7Mn-TRIP steel in Poling's work [76], the ultimate tensile strength, ductility, work hardening rate and transformation rate all decreased with an increase in strain rate. However, these UFG medium-Mn TRIP steels [76,121–123] also showed evidence of PLC bands during tensile deformation, which was similarly associated with a negative strain rate sensitivity of the UTS due to a strong dependence on the adiabatic heating. In most studies on UFG medium-Mn TRIP steels

[76,121–123] and even in the case of coarse-grained high-Mn TWIP steels [124], the PLC bands disappear at high strain rates, which leads to negative strain rate sensitivities of the UTS.

### 4.3 Crystal plasticity finite element modeling and parametric investigations

The CPFE simulation incorporates tensile properties using the Taylor model [125] and focuses on the driving forces of plasticity within the multi-phase material, but does not consider grain morphology or grain interactions. The advantage of combining a range of empirical measurements (high-rate tensile tests, DIC, thermal imaging, DF-TEM, and EBSD) with a CPFE model is a detailed understanding of the mechanical behavior and microstructural influences for a given material condition. For example, the strain-rate sensitivity of this material is captured in the thermal activation [volume and energy barriers] of FCC and BCC crystals [94][126]. The use of constitutive equations in the CPFE model enables a user to calibrate the high strain-rate behavior of the multi-phase TWIP-TRIP steel and allows for a parametric analysis of the calibrated variables. As AHSS forming operations and automotive crash settings experience strain rates in the range of  $\dot{\epsilon} = 10^{-2}$  s<sup>-1</sup> to  $\dot{\epsilon} = 10^3$  s<sup>-1</sup> [28,29], strain rate sensitivity of a given material should be incorporated during alloy design of next-generation automotive steels. AHSS design strategies typically employ thermodynamic simulations, ab initio simulations, and composite models to predict areas of opportunity [1,42,43,127]. Based on results from the current work, a parametric analysis allows for prediction of tensile properties outside the experimental regime by using a microstructure-based CPFE model and tuning one variable at a time. In comparison, changing the intercritical annealing temperature for medium-Mn steels affects multiple variables at once such as phase fraction, grain size, grain morphology, recovery or recrystallization of martensite, austenite thermal stability, austenite composition (C and Mn content) and stacking fault energy, austenite transformation rate, and thus mechanical properties.

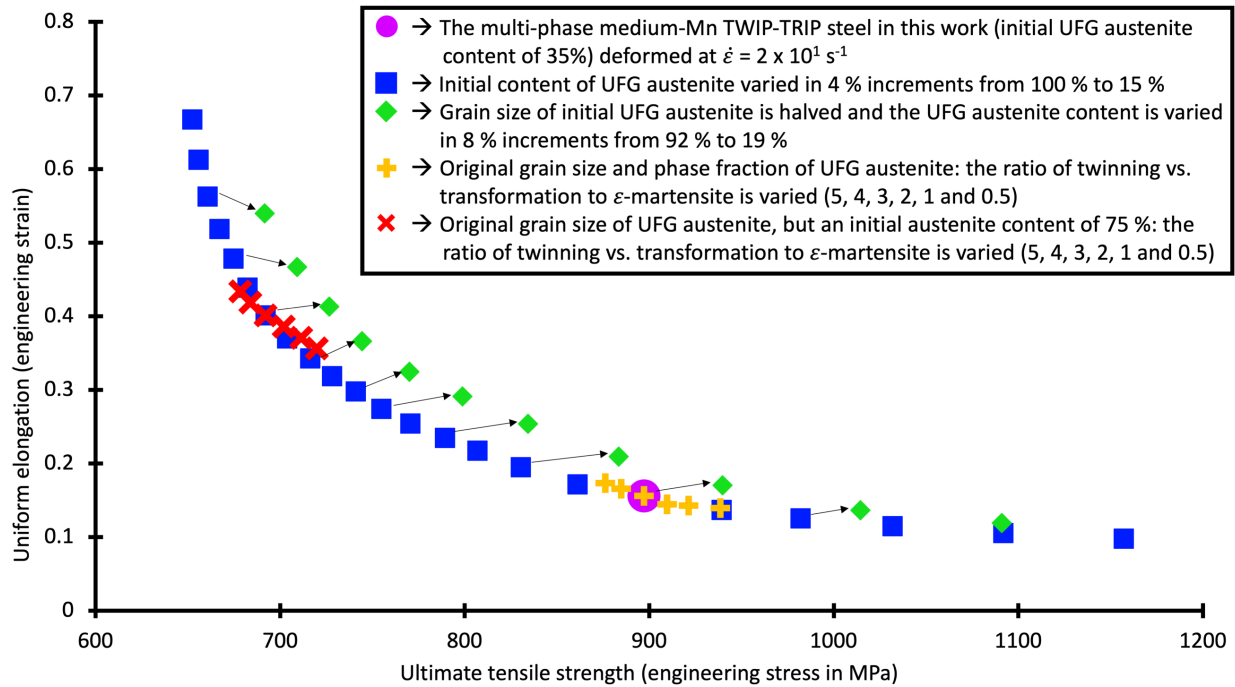


Figure 9: Parametric analysis using calibrated parameters from the present work deformed at  $\dot{\epsilon} = 2 \times 10^1 \text{ s}^{-1}$  (a single circle). The CPFE model in this work is used to predict mechanical properties outside the experimental regime using variations in austenite fraction (squares), austenite grain size (diamonds are linked to respective austenite fractions with arrows) and ratio of twinning vs. transformation to  $\epsilon$ -martensite (5, 4, 3, 2, 1, 0.5 indicated by X's and +'s).

The parametric analysis completed for this work is plotted in terms of UTS and UE on a linear scale (see Figure 9) to highlight contributions to the literature. The product of UTS and total elongation is typically reported in literature [2,3]. A parameter relevant to this work is the product of UTS in engineering stress and % UE in engineering strain because uniform elongation does not consider the necking behavior. As such, UE and UTS can be accurately represented by a single RVE. In many cases, the use of a single RVE is used in the modeling community to simulate uniaxial tension of a given microstructure [46].

Physical parameters relevant for AHSS alloy design are varied in Figure 9. Manipulating phase fraction in multi-phase steels typically has as a composite effect on mechanical properties [3]. Phase fraction in medium-Mn steels can be controlled by both annealing temperature and annealing time [11]. The circle in Figure 9 denotes the UTS and % UE (using engineering stress-strain values) of the cold-rolled and annealed multi-phase medium-Mn TWIP-TRIP steel deformed at  $\dot{\epsilon} = 2 \times 10^1 \text{ s}^{-1}$ . The squares in Figure 9 provide a range of initial austenite % from 15 % to 100 %. Generally, increasing the initial fraction of austenite increases the uniform engineering strain and decreases the ultimate tensile strength. For example, increasing the amount of initial UFG austenite from 23 % (UTS = 1032 MPa, UE = 0.115) to 55 % (UTS = 770 MPa, UE = .254) increases the product of UTS and % UE from  $1.18 \times 10^4 \text{ MPa}\%$  to  $1.96 \times 10^4 \text{ MPa}\%$  due to the higher strain hardening capacity of austenite. Notably, the parametric study predicts only a minimal decrease in % UE when the amount of initial UFG austenite changes from 27 % to 15 %.

Austenite grain size can be controlled experimentally by annealing temperature and time as the reverted austenite grows [33]. The size of the UF austenite grains influences the strength of this multi-phase material through a Hall-Petch effect [99]. In the current model, the smaller grain size of polycrystalline austenite requires more dislocation activation to achieve a given magnitude of plastic strain. Reducing the austenite grain size increases resistance to deformation and thus strength. The diamonds in Figure 9 represent the predicted mechanical properties of the multi-phase material if the austenite grain size is halved. The arrows between the squares and diamonds correspond to the same initial phase fraction of austenite. In the case of 92 % initial UFG austenite (UTS = 660 MPa, UE = 0.563), halving the grain size of the already UFG austenite results in slight reduction in UE (0.539) and a marginal increase in UTS (691 MPa). The largest increase in UTS from simply halving the grain size of UFG austenite occurs when the initial amount of austenite (prior to deformation) is 43 % (UTS changes from 830 MPa to 890 MPa).

Generally, more twinning (a greater ratio of twinning vs. transformation to  $\epsilon$ -martensite) leads to greater amounts of uniform elongation. The difference in the amount of strain-induced mechanical twinning vs. the amount of strain-induced  $\epsilon$ -martensite (both are planar defects) is typically characterized by a change in austenite stacking fault energy and can be tuned by varying composition and intercritical annealing temperature [17,116]. For the predicted material condition containing 75 % initial austenite, a change in the ratio of twinning vs. transformation to  $\epsilon$ -martensite from 5 (more twinning) to 0.5 (more  $\epsilon$ -martensite) results in an increase in UTS from 678 MPa to 720 MPa and a decrease in UE from 0.433 to 0.356 (see X's in Figure 9). With reference to the measured mechanical properties (initial austenite fraction of 35 %), a decrease in

initial austenite fraction from 35 to 31% (see the square to the right of the circle in Figure 9) results in the same predicted mechanical properties (UTS = 939 MPa, UE = 0.139) as a decrease in the ratio of twinning vs. transformation to  $\varepsilon$ -martensite from 3 to 0.5.

By coupling CPFE models with experimental measurements (such as EBSD and TEM) a desired set of high strain rate mechanical properties in medium-Mn steels may be achieved more efficiently by including a parametric study during alloy design, rather exploring results from multiple processing steps. Future parametric studies could also include in situ measurements of twin fraction evolution and austenite transformation rates (as opposed to post mortem measurements) to better inform the constitutive model [13,128–130].

## 5. Conclusions

1. The unique multi-phase microstructure (comprised of many sizes and morphologies) and low C content of a cold-rolled and annealed medium-Mn TWIP-TRIP steel suppresses static and dynamic strain aging effects, which results in a positive strain rate sensitivity of both the yield strength and ultimate tensile strength (from  $\dot{\varepsilon} = 2 \times 10^{-4} \text{ s}^{-1}$  to  $\dot{\varepsilon} = 2 \times 10^2 \text{ s}^{-1}$ ). As automotive parts become more complex, next generation steel design strategies will continue to advance when localized plastic instabilities are subdued.
2. By coupling advanced empirical measurements and state-of-the-art computational approaches, mechanical properties of complex materials can be calibrated with high fidelity across a large range of strain rates. Our parametric analysis provides insight into how high strain rate mechanical properties can be tuned (outside the experimental regime) by manipulating a specific set of microstructural parameters that are most relevant to conventional alloy design practices.

## Acknowledgements

This work was funded by the United States National Science Foundation (US-NSF) Division of Materials Research under grant DMR1309258, US-NSF EPS 1004083 and the Max Planck Institut für Eisenforschung in Düsseldorf, Germany. Servo-hydraulic tension testing, digital image correlation, and thermal imaging was completed in the NIST Center for Automotive Lightweighting at the National Institute of Standards and Technology in Gaithersburg, MD. CPFE simulations were completed at the Multi-scale Modeling and Simulation center at Vanderbilt University. The authors are grateful for fruitful discussions with Steve Mates (NIST-Gaithersburg).

## References

- [1] D.K. Matlock, J.G. Speer, Processing Opportunities for New Advanced High-Strength Sheet Steels, *Mater. Manuf. Process.* 25:1–3 (2010) 7–13. doi:10.1080/10426910903158272.
- [2] Y.-K. Lee, J. Han, Current opinion in medium manganese steel, *Mater. Sci. Technol.* 31 (2015) 843–856. doi:10.1179/1743284714Y.0000000722.
- [3] D.K. Matlock, J.G. Speer, Third generation of AHSS: microstructure design concepts, in: A. Haldar, S. Suwas, D. Bhattacharjee (Eds.), *Microstruct. Texture Steels*, Springer, London, 2009: pp. 185–205. doi:10.1007/978-1-84882-454-6\_11.
- [4] F.B. Pickering, Toward Improved Toughness and Ductility, *Climax Molybdenum Dev. Co.* (1971) 9–32.

- [5] D.K. Matlock, G. Krauss, F. Zia-Ebrahimi, Deformation, Processing and Structure, ASM, Met. Park. OH. (1984) 47–87.
- [6] D.M. Field, J. Qing, D.C. van Aken, Chemistry and Properties of Medium-Mn Two-Stage TRIP Steels, *Metall. Mater. Trans. A Phys. Metall. Mater. Sci.* (2018) 1–18. doi:10.1007/s11661-018-4798-6.
- [7] M. Kuzmina, M. Herbig, D. Ponge, S. Sandlobes, D. Raabe, Linear complexions: Confined chemical and structural states at dislocations, *Science* (80-). 349 (2015) 1080–1083. doi:10.1126/science.aab2633.
- [8] J. Han, A.K. da Silva, D. Ponge, D. Raabe, S.M. Lee, Y.K. Lee, S.I. Lee, B. Hwang, The effects of prior austenite grain boundaries and microstructural morphology on the impact toughness of intercritically annealed medium Mn steel, *Acta Mater.* 122 (2017) 199–206. doi:10.1016/j.actamat.2016.09.048.
- [9] S. Lee, B.C. De Cooman, Annealing Temperature Dependence of the Tensile Behavior of 10 pct Mn Multi-phase TWIP-TRIP Steel, *Metall. Mater. Trans. A*. 45 (2014) 6039–6052. doi:10.1007/s11661-014-2540-6.
- [10] S. Lee, S.J. Lee, S. Santhosh Kumar, K. Lee, B.C.D. Cooman, Localized deformation in multiphase, ultra-fine-grained 6 Pct Mn transformation-induced plasticity steel, *Metall. Mater. Trans. A*. 42 (2011) 3638–3651. doi:10.1007/s11661-011-0636-9.
- [11] S. Lee, B.C. De Cooman, On the selection of the optimal intercritical annealing temperature for medium Mn TRIP steel, *Metall. Mater. Trans. A*. 44 (2013) 5018–5024. doi:10.1007/s11661-013-1860-2.
- [12] S. Lee, K. Lee, B.C. de Cooman, Observation of the TWIP + TRIP Plasticity-Enhancement Mechanism in Al-Added 6 Wt Pct Medium Mn Steel, *Metall. Mater. Trans. A*. (2015) 1–8. doi:10.1007/s11661-015-2854-z.
- [13] S. Lee, W. Woo, B.C. de Cooman, Analysis of the Tensile Behavior of 12 pct Mn Multi-phase ( $\alpha$  +  $\gamma$ ) TWIP + TRIP Steel by Neutron Diffraction, *Metall. Mater. Trans. A*. 47 (2016) 2125–2140. doi:10.1007/s11661-016-3407-9.
- [14] C. Wang, W. Cao, J. Shi, C. Huang, H. Dong, Deformation microstructures and strengthening mechanisms of an ultrafine grained duplex medium-Mn steel, *Mater. Sci. Eng. A*. 562 (2013) 89–95. doi:10.1016/j.msea.2012.11.044.
- [15] R. Zhang, W.Q. Cao, Z.J. Peng, J. Shi, H. Dong, C.X. Huang, Intercritical rolling induced ultra fine microstructure and excellent mechanical properties of the medium-Mn steel, *Mater. Sci. Eng. A*. 583 (2013) 84–88. doi:10.1016/j.msea.2013.06.067.
- [16] M.C. McGrath, D.C. Van Aken, N.I. Medvedeva, J.E. Medvedeva, Work hardening behavior in steel with multiple TRIP mechanisms, *Metall. Mater. Trans. A*. 44 (2013) 4634–4643. doi:10.1007/s11661-013-1820-x.
- [17] D.T. Pierce, J.A. Jiménez, J. Bentley, D. Raabe, J.E. Wittig, The influence of stacking fault energy on the microstructural and strain-hardening evolution of Fe-Mn-Al-Si steels during tensile deformation, *Acta Mater.* 100 (2015) 178–190. doi:10.1016/j.actamat.2015.08.030.
- [18] S. Curtze, V.T. Kuokkala, Dependence of tensile deformation behavior of TWIP steels on stacking fault energy, temperature and strain rate, *Acta Mater.* 58 (2010) 5129–5141. doi:10.1016/j.actamat.2010.05.049.
- [19] D.T. Pierce, J.A. Jimenez, J. Bentley, D. Raabe, C. Oskay, J.E. Wittig, The influence of manganese content on the stacking fault and austenite/epsilon-martensite interfacial energies in Fe-Mn-(Al-Si) steels investigated by experiment and theory, *Acta Mater.* 68 (2014) 238–253. doi:10.1016/j.actamat.2014.01.001.
- [20] O. Grässel, G. Frommeyer, C. Derder, H. Hofmann, Phase Transformations and Mechanical Properties of Fe-Mn-Si-Al TRIP-Steels, *Le J. Phys. IV*. 07 (1997) 383–388. doi:10.1051/jp4:1997560.
- [21] S. Allain, J.P. Chateau, O. Bouaziz, S. Migot, N. Guelton, Correlations between the calculated stacking fault energy and the plasticity mechanisms in Fe-Mn-C alloys, *Mater. Sci. Eng. A*. 387–

- 389 (2004) 158–162. doi:10.1016/j.msea.2004.01.059.
- [22] A. Dumay, J.P. Chateau, S. Allain, S. Migot, O. Bouaziz, Influence of addition elements on the stacking-fault energy and mechanical properties of an austenitic Fe-Mn-C steel, *Mater. Sci. Eng. A* 483–484 (2008) 184–187. doi:10.1016/j.msea.2006.12.170.
- [23] A. Saeed-Akbari, J. Imlau, U. Prahl, W. Bleck, Derivation and variation in composition-dependent stacking fault energy maps based on subregular solution model in high-manganese steels, *Metall. Mater. Trans. A Phys. Metall. Mater. Sci.* 40 (2009) 3076–3090. doi:10.1007/s11661-009-0050-8.
- [24] M. Pozuelo, J.E. Wittig, J.A. Jiménez, G. Frommeyer, Enhanced mechanical properties of a novel high-nitrogen Cr-Mn-Ni-Si austenitic stainless steel via TWIP/TRIP effects, *Metall. Mater. Trans. A Phys. Metall. Mater. Sci.* 40 (2009) 1826–1834. doi:10.1007/s11661-009-9863-8.
- [25] J.T. Benzing, W.A. Poling, D.T. Pierce, J. Bentley, K.O. Findley, D. Raabe, J.E. Wittig, Effects of strain rate on mechanical properties and deformation behavior of an austenitic Fe-25Mn-3Al-3Si TWIP-TRIP steel, *Mater. Sci. Eng. A* 711 (2018) 78–92. doi:10.1016/j.msea.2017.11.017.
- [26] J.T. Benzing, A. Kwiatkowski da Silva, L. Morsdorf, J. Bentley, D. Ponge, A. Dutta, J. Han, J.R. McBride, B. Van Leer, B. Gault, D. Raabe, J.E. Wittig, Multi-scale characterization of austenite reversion and martensite recovery in a cold-rolled medium-Mn steel, *Acta Mater.* 166 (2019) 512–530. doi:10.1016/j.actamat.2019.01.003.
- [27] J.T. Benzing, J. Bentley, J.R. McBride, D. Ponge, J. Han, D. Raabe, J.E. Wittig, Characterization of Partitioning in a Medium-Mn Third-Generation AHSS, *Microsc. Microanal.* 23 Suppl 1 (2017) 402–403. doi:10.1017/S1431927617002690.
- [28] M. Seth, V.J. Vohnout, G.S. Daehn, Formability of steel sheet in high velocity impact, *J. Mater. Process. Technol.* 168 (2005) 390–400. doi:10.1016/j.jmatprotec.2004.08.032.
- [29] S. Hiermaier, *Structures Under Crash and Impact: Continuum Mechanics, Discretization and Experimental Characterization*, New York, 2008.
- [30] S.J. Lee, J. Kim, S.N. Kane, B.C. De Cooman, On the origin of dynamic strain aging in twinning-induced plasticity steels, *Acta Mater.* 59 (2011) 6809–6819. doi:10.1016/j.actamat.2011.07.040.
- [31] M. Callahan, O. Hubert, F. Hild, A. Perlade, J.H. Schmitt, Coincidence of strain-induced TRIP and propagative PLC bands in Medium Mn steels, *Mater. Sci. Eng. A* 704 (2017) 391–400. doi:10.1016/j.msea.2017.08.042.
- [32] Z.H. Cai, S.Y. Jing, H.Y. Li, K.M. Zhang, R.D.K. Misra, H. Ding, Z.Y. Tang, The influence of microstructural characteristics on yield point elongation phenomenon in Fe-0.2C-11Mn-2Al steel, *Mater. Sci. Eng. A* 739 (2019) 17–25. doi:10.1016/j.msea.2018.09.114.
- [33] Y. Zhang, L. Wang, K.O. Findley, J.G. Speer, Influence of Temperature and Grain Size on Austenite Stability in Medium Manganese Steels, *Metall. Mater. Trans. A* 48 (2017) 2140–2149. doi:10.1007/s11661-017-3995-z.
- [34] X.G. Wang, L. Wang, M.X. Huang, Kinematic and thermal characteristics of Lüders and Portevin-Le Châtelier bands in a medium Mn transformation-induced plasticity steel, *Acta Mater.* 124 (2017) 17–29. doi:10.1016/j.actamat.2016.10.069.
- [35] B. Sun, N. Vanderesse, F. Fazeli, C. Scott, J. Chen, P. Bocher, M. Jahazi, S. Yue, Discontinuous strain-induced martensite transformation related to the Portevin-Le Chatelier effect in a medium manganese steel, *Scr. Mater.* 133 (2017) 9–13. doi:10.1016/j.scriptamat.2017.01.022.
- [36] H. Luo, H. Dong, M. Huang, Effect of intercritical annealing on the Lüders strains of medium Mn transformation-induced plasticity steels, *Mater. Des.* 83 (2015) 42–48. doi:10.1016/j.matdes.2015.05.085.
- [37] H. Aboulfadil, J. Deges, P. Choi, D. Raabe, Dynamic strain aging studied at the atomic scale, *Acta Mater.* 86 (2015) 34–42. doi:10.1016/j.actamat.2014.12.028.
- [38] E. Emadoddin, A. Akbarzadeh, G.H. Daneshi, Correlation between Lüder strain and retained austenite in TRIP-assisted cold rolled steel sheets, *Mater. Sci. Eng. A* 447 (2007) 174–179. doi:10.1016/j.msea.2006.10.046.
- [39] M.T. Kim, T.M. Park, K.H. Baik, W.S. Choi, J. Han, Effects of cold rolling reduction ratio on microstructures and tensile properties of intercritically annealed medium-Mn steels, *Mater. Sci.*

- Eng. A. 752 (2019) 43–54. doi:10.1016/j.msea.2019.02.091.
- [40] H. Wang, Y. Zhang, G. Yuan, J. Kang, Y. Wang, R.D.K. Misra, G. Wang, Significance of cold rolling reduction on Lüders band formation and mechanical behavior in cold-rolled intercritically annealed medium-Mn steel, Mater. Sci. Eng. A. 737 (2018) 176–181. doi:10.1016/j.msea.2018.09.045.
- [41] W.A. Poling, K.O. Findley, E. De Moor, Deformation of Third Generation Advanced High Strength Sheet Steels Under High Strain Rates, Color. Sch. Mines, ASPPRC Res. Rep. MT-SRC-014 (2014).
- [42] P.J. Gibbs, Design considerations for the third generation advanced high strength steel, Colorado School of Mines, 2012.
- [43] S.T. Mileiko, The tensile strength and ductility of continuous fibre composites, J. Mater. Sci. 4 (1969) 974–977. doi:10.1007/BF00555312.
- [44] A. Ma, A. Hartmaier, A study of deformation and phase transformation coupling for TRIP-assisted steels, Int. J. Plast. 64 (2015) 40–55. doi:10.1016/j.ijplas.2014.07.008.
- [45] M.I. Latypov, S. Shin, B.C. De Cooman, H.S. Kim, Micromechanical finite element analysis of strain partitioning in multiphase medium manganese TWIP+TRIP steel, Acta Mater. 108 (2016) 219–228. doi:10.1016/j.actamat.2016.02.001.
- [46] F. Roters, P. Eisenlohr, L. Hantcherli, D.D. Tjahjanto, T.R. Bieler, D. Raabe, Overview of constitutive laws, kinematics, homogenization and multiscale methods in crystal plasticity finite-element modeling: Theory, experiments, applications, Acta Mater. 58 (2010) 1152–1211. doi:10.1016/j.actamat.2009.10.058.
- [47] B. Hu, H. Luo, F. Yang, H. Dong, Recent progress in medium-Mn steels made with new designing strategies, a review, J. Mater. Sci. Technol. (2017) 6–13. doi:10.1016/j.jmst.2017.06.017.
- [48] P.J. Gibbs, E. De Moor, M.J. Merwin, B. Clausen, J.G. Speer, D.K. Matlock, Austenite stability effects on tensile behavior of manganese-enriched- austenite transformation-induced plasticity steel, Metall. Mater. Trans. A Phys. Metall. Mater. Sci. 42 (2011) 3691–3702. doi:10.1007/s11661-011-0687-y.
- [49] Y. Ma, W. Song, S. Zhou, A. Schwedt, W. Bleck, Influence of Intercritical Annealing Temperature on Microstructure and Mechanical Properties of a Cold-Rolled Medium-Mn Steel, Metals (Basel). 8 (2018) 357. doi:10.3390/met8050357.
- [50] H. Lee, M.C. Jo, S.S. Sohn, A. Zargaran, J.H. Ryu, N.J. Kim, S. Lee, Novel medium-Mn (austenite + martensite) duplex hot-rolled steel achieving 1.6 GPa strength with 20 % ductility by Mn-segregation-induced TRIP mechanism, Acta Mater. 147 (2018) 247–260. doi:10.1016/j.actamat.2018.01.033.
- [51] M. Borsutzki, D. Cornette, Y. Kuriyama, A. Uenishi, B. Yan, E. Oproeck, Recommendations for Dynamic Tensile Testing of Sheet Steels, Intern. Iron Steel Inst. (2005).
- [52] P. Eisenlohr, D.D. Tjahjanto, T. Hochrainer, F. Roters, D. Raabe, Comparison of texture evolution in fcc metals predicted by various grain cluster homogenization schemes, Int. J. Mater. Res. 100 (2009) 500–509. doi:10.3139/146.110071.
- [53] X. Zhang, C. Oskay, Sparse and scalable eigenstrain-based reduced order homogenization models for polycrystal plasticity, Comput. Methods Appl. Mech. Eng. 326 (2017) 241–269. doi:10.1016/j.cma.2017.07.027.
- [54] D.D. Tjahjanto, S. Turteltaub, A.S.J. Suiker, Crystallographically based model for transformation-induced plasticity in multiphase carbon steels, Contin. Mech. Thermodyn. 19 (2008) 399–422. doi:10.1007/s00161-007-0061-x.
- [55] B. Mohammed, T. Park, F. Pourboghrat, J. Hu, R. Esmaeilpour, F. Abu-Farha, Multiscale crystal plasticity modeling of multiphase advanced high strength steel, Int. J. Solids Struct. 151 (2018) 57–75. doi:10.1016/j.ijsolstr.2017.05.007.
- [56] O. Bouaziz, S. Allain, C. Scott, Effect of grain and twin boundaries on the hardening mechanisms of twinning-induced plasticity steels, Scr. Mater. 58 (2008) 484–487. doi:10.1016/j.scriptamat.2007.10.050.

- [57] O. Bouaziz, P. Buessler, Iso-work Increment Assumption for Heterogeneous Material Behaviour Modelling, *Adv. Eng. Mater.* 6 (2004) 79–83. doi:10.1002/adem.200300524.
- [58] S. Lee, Y. Estrin, B.C. De Cooman, Constitutive modeling of the mechanical properties of V-added medium manganese TRIP steel, *Metall. Mater. Trans. A Phys. Metall. Mater. Sci.* 44 (2013) 3136–3146. doi:10.1007/s11661-013-1648-4.
- [59] L. Samek, E. De Moor, J. Penning, B.C. Cooman, Influence of Alloying Elements on the Kinetics of Strain-Induced Martensitic Nucleation in Low-Alloy, Multiphase High-Strength Steels, *Metall. Mater. Trans. A*, 37 (2006) 109–124. doi:10.1007/s11661-006-0157-0.
- [60] S. Kibey, J.B. Liu, D.D. Johnson, H. Sehitoglu, Predicting twinning stress in fcc metals: Linking twin-energy pathways to twin nucleation, *Acta Mater.* 55 (2007) 6843–6851. doi:10.1016/j.actamat.2007.08.042.
- [61] S. Lee, Y. Estrin, B.C. De Cooman, Effect of the strain rate on the TRIP-TWIP transition in austenitic Fe-12 pct Mn-0.6 pct C TWIP Steel, *Metall. Mater. Trans. A Phys. Metall. Mater. Sci.* 45 (2014) 717–730. doi:10.1007/s11661-013-2028-9.
- [62] H. Idrissi, K. Renard, L. Ryelandt, D. Schryvers, P.J. Jacques, On the mechanism of twin formation in Fe-Mn-C TWIP steels, *Acta Mater.* 58 (2010) 2464–2476. doi:10.1016/j.actamat.2009.12.032.
- [63] S. Miura, J.I. Takamura, N. Narita, Orientation Dependence of Flow Stress for Twinning in Silver Crystals, *Trans. Jpn. Int. Met. Inst. Met. S* (1968) 555.
- [64] J.B. Cohen, J. Weertman, A Dislocation Model for Twinning in F.C.C. Metals, *Acta Met.* 11 (1963) 996–998.
- [65] B.C. De Cooman, Y. Estrin, S.K. Kim, Twinning-induced plasticity (TWIP) steels, *Acta Mater.* 142 (2018) 283–362. doi:10.1016/j.actamat.2017.06.046.
- [66] A. Saeed-Akbari, L. Mosecker, A. Schwedt, W. Bleck, Characterization and prediction of flow behavior in high-manganese twinning induced plasticity steels: Part i. mechanism maps and work-hardening behavior, *Metall. Mater. Trans. A*, 43 (2012) 1688–1704. doi:10.1007/s11661-011-0993-4.
- [67] O. Grässel, L. Krüger, G. Frommeyer, L.W. Meyer, High strength Fe-Mn-(Al, Si) TRIP/TWIP steels development - properties - application, *Int. J. Plast.* 16 (2000) 1391–1409. doi:10.1016/S0749-6419(00)00015-2.
- [68] S.L. Wong, M. Madivala, U. Prahl, F. Roters, D. Raabe, A crystal plasticity model for twinning-and transformation-induced plasticity, *Acta Mater.* 118 (2016) 140–151. doi:10.1016/j.actamat.2016.07.032.
- [69] D.R. Steinmetz, T. Jäpel, B. Wietbrock, P. Eisenlohr, I. Gutierrez-Urrutia, A. Saeed-Akbari, T. Hickel, F. Roters, D. Raabe, Revealing the strain-hardening behavior of twinning-induced plasticity steels: Theory, simulations, experiments, *Acta Mater.* 61 (2013) 494–510. doi:10.1016/j.actamat.2012.09.064.
- [70] T. Jøssang, J.P. Hirth, C.S. Hartley, Anisotropic elasticity solutions for dislocation barriers in face-centered cubic crystals, *J. Appl. Phys.* 36 (1965) 2400–2406. doi:10.1063/1.1714498.
- [71] R.E. Reed-Hill, R. Abbaschian, *Physical Metallurgy Principles*, Third ed, PWS Publishing Company, Boston, 1994.
- [72] D.T. Pierce, *The Influence of Manganese Content and Temperature on the Relative FCC/HCP Phase Stability and Strain-Hardening Behavior of High-Manganese TRIP/TWIP Steels*, Vanderbilt University, 2014.
- [73] S. Mahajan, Critique of mechanisms of formation of deformation, annealing and growth twins: Face-centered cubic metals and alloys, *Scr. Mater.* 68 (2013) 95–99. doi:10.1016/j.scriptamat.2012.09.011.
- [74] G.B. Olson, M. Cohen, A general mechanism of martensitic nucleation: Part I. General concepts and the FCC → HCP transformation, *Metall. Trans. A*, 7 (1976) 1897–1904. doi:10.1007/BF02654987.
- [75] S. Lee, B.C. De Cooman, Tensile Behavior of Intercritically Annealed 10 pct Mn Multi-phase

- Steel, Metall. Mater. Trans. A. 45 (2014) 709–716. doi:10.1007/s11661-013-2047-6.
- [76] Poling; W., Tensile Deformation of Third Generation Advanced High Strength Sheet Steels Under High Strain Rates, Ph.D. dissertation, Colorado School of Mines, 2016.
- [77] D.T. Pierce, J. Bentley, J.A. Jimenez, J.E. Wittig, The Influence of Stacking-Fault Energy on Deformation Mechanisms in an Fe- Mn-Al-Si Austenitic TRIP / TWIP Steel, 18 (2012) 1894–1895. doi:10.1017/S1431927612011324.
- [78] I.R. Souza Filho, M.J.R. Sandim, D. Ponge, H.R.Z. Sandim, D. Raabe, Strain hardening mechanisms during cold rolling of a high-Mn steel: Interplay between submicron defects and microtexture, Mater. Sci. Eng. A. 754 (2019) 636–649. doi:10.1016/J.MSEA.2019.03.116.
- [79] T. Angel, Formation of Martensite in Austenitic Stainless Steel, J. Iron Steel Inst. 177 (1954) 165–174.
- [80] D.C. Ludwigson, J.A. Berger, Plastic Behavior of Metastable Austenitic Stainless Steels, J. Iron Steel Inst. 207 (1969) 69–75.
- [81] J. Burke, Kinetics of Phase Transformation in Metals, Pergamon Press, Oxford, United Kingdom, 1965.
- [82] O. Matsumura, Y. Sakuma, H. Takech, TRIP and its kinetic aspects in austempered 0.4C–1.5Si–0.8Mn steel, Scr. Metall. Mater. 21 (1987) 1301–1306.
- [83] N. Tsuchida, Y. Tomota, A micromechanic modeling for transformation induced plasticity in steels, Mater. Sci. Eng. A285 (2000) 345–352.
- [84] K. Sugimoto, M. Kobayashi, S. Hashimoto, Ductility and Strain-Induced Transformation in a High-Strength Transformation -Induced Plasticity-Aided Dual-Phase Steel, Metall. Mater. Trans. A. 23A (1992) 3085–3091.
- [85] I.Y. Pychmintsev, R.A. Savrai, B.C. De Cooman, O. Moriau, High strain rate behavior of TRIP-aided automotive steels, in: Int. Conf. TRIP-Aided High Strength Ferr. Alloy., 2002: pp. 299–302.
- [86] W.W. Gerberich, G. Thomas, E.R. Parker, V.F. Zackay, Metastable Austenites: Decomposition and Strength, in: 2nd Int. Conf. Strength Met. Alloy. ASM, Metals Park, OH, 1970: pp. 894–99.
- [87] J.R. Guimarães, The deformation-induced martensitic reaction in polycrystalline Fe-30.7Ni-0.06C, Scr. Metall. Mater. 6 (1972) 795–803.
- [88] C.Y. Sun, N. Guo, M.W. Fu, S.W. Wang, Modeling of slip, twinning and transformation induced plastic deformation for TWIP steel based on crystal plasticity, Int. J. Plast. 76 (2016) 186–212. doi:10.1016/j.ijplas.2015.08.003.
- [89] M.G. Lee, S.J. Kim, H.N. Han, Crystal plasticity finite element modeling of mechanically induced martensitic transformation (MIMT) in metastable austenite, Int. J. Plast. 26 (2010) 688–710. doi:10.1016/j.ijplas.2009.10.001.
- [90] A.S.J. Suiker, S. Turteltaub, Computational modelling of plasticity induced by martensitic phase transformations, Int. J. Numer. Methods Eng. 63 (2005) 1655–1693. doi:10.1002/nme.1327.
- [91] S.R. Kalidindi, C.A. Bronkhorst, L. Anand, Crystallographic texture evolution in bulk deformation processing of FCC metals, J. Mech. Phys. Solids. (1992). doi:10.1016/0022-5096(92)80003-9.
- [92] G.Y. Chin, W.F. Hosford, D.R. Mendorf, Accommodation of Constrained Deformation in f.c.c. Metals by Slip and Twinning, Proc. R. Soc. Lond. A. Math. Phys. Sci. 309 (1969) 433–456. <http://www.jstor.org/stable/2416097>.
- [93] S.R. Kalidindi, Modeling anisotropic strain hardening and deformation textures in low stacking fault energy fcc metals, Int. J. Plast. (2001). doi:10.1016/S0749-6419(00)00071-1.
- [94] P. Hu, Y. Liu, Y. Zhu, L. Ying, Crystal plasticity extended models based on thermal mechanism and damage functions: Application to multiscale modeling of aluminum alloy tensile behavior, Int. J. Plast. 86 (2016) 1–25. doi:10.1016/j.ijplas.2016.07.001.
- [95] Y. Liu, Y. Zhu, C. Oskay, P. Hu, L. Ying, D. Wang, Experimental and computational study of microstructural effect on ductile fracture of hot-forming materials, Mater. Sci. Eng. A. 724 (2018) 298–323. doi:10.1016/j.msea.2018.03.049.
- [96] G.I. Taylor, H. Quinney, The Latent Energy Remaining in a Metal after Cold Working, Proc. R. Soc. London. Ser. A, Contain. Pap. a Math. Phys. Character. 143 (1934) 307–326.

- doi:10.1098/rspa.1934.0004.
- [97] S. Klitschke, A. Trondl, F. Huberth, M. Liewald, Adiabatic heating under various loading situations and strain rates for advanced high-strength steels, IOP Conf. Ser. Mater. Sci. Eng. 418 (2018) 12123. doi:10.1088/1757-899X/418/1/012123.
- [98] R. Zaera, J.A. Rodríguez-Martínez, D. Rittel, On the Taylor-Quinney coefficient in dynamically phase transforming materials. Application to 304 stainless steel, Int. J. Plast. 40 (2013) 185–201. doi:10.1016/j.ijplas.2012.08.003.
- [99] I.J. Beyerlein, C.N. Tomé, A dislocation-based constitutive law for pure Zr including temperature effects, Int. J. Plast. 24 (2008) 867–895. doi:10.1016/j.ijplas.2007.07.017.
- [100] R. Madec, B. Devincre, L.P. Kubin, From Dislocation Junctions to Forest Hardening, Phys. Rev. Lett. 89 (2002) 255508. doi:10.1103/PhysRevLett.89.255508.
- [101] U.F. Kocks, A.. Argon, M.F. Ashby, Thermodynamics and kinetics of slip, Pergamon Press, 1975.
- [102] G.E. Dieter, Mechanical Metallurgy, page 297, 3rd ed., McGraw-Hill, Boston, 1986.
- [103] D.T. Pierce, K. Nowag, A. Montagne, J.A. Jiménez, J.E. Wittig, R. Ghisleni, Single crystal elastic constants of high-manganese transformation- and twinning-induced plasticity steels determined by a new method utilizing nanoindentation, Mater. Sci. Eng. A. 578 (2013) 134–139. doi:10.1016/j.msea.2013.04.049.
- [104] M. Haupt, A. Dutta, D. Ponge, S. Sandlöbes, M. Nellessen, G. Hirt, Influence of Intercritical Annealing on Microstructure and Mechanical Properties of a Medium Manganese Steel, Procedia Eng. 207 (2017) 1803–1808. doi:10.1016/j.proeng.2017.10.942.
- [105] M.M. Wang, C.C. Tasan, D. Ponge, D. Raabe, Spectral TRIP enables ductile 1.1 GPa martensite, Acta Mater. 111 (2016) 262–272. doi:10.1016/j.actamat.2016.03.070.
- [106] A. Dutta, D. Ponge, S. Sandlöbes, D. Raabe, Strain partitioning and strain localization in medium manganese steels measured by in situ microscopic digital image correlation, Materialia. (2019) 100252. doi:10.1016/j.mtla.2019.100252.
- [107] Y. Ma, Medium-manganese steels processed by austenite-reverted-transformation annealing for automotive applications, Mater. Sci. Technol. 33 (2017) 1713–1727. doi:10.1080/02670836.2017.1312208.
- [108] R.L. Miller, Ultrafine-grained microstructures and mechanical properties of alloy steels, Metall. Trans. 3 (1972) 905–912. doi:10.1007/BF02647665.
- [109] J. Han, S.H. Kang, S.J. Lee, Y.K. Lee, Fabrication of bimodal-grained Al-free medium Mn steel by double intercritical annealing and its tensile properties, J. Alloys Compd. 681 (2016) 580–588. doi:10.1016/j.jallcom.2016.04.014.
- [110] B.C. De Cooman, P. Gibbs, S. Lee, D.K. Matlock, Transmission electron microscopy analysis of yielding in ultrafine-grained medium Mn transformation-induced plasticity steel, Metall. Mater. Trans. A. 44 (2013) 2563–2572. doi:10.1007/s11661-013-1638-6.
- [111] P.J. Gibbs, B.C. De Cooman, D.W. Brown, B. Clausen, J.G. Schroth, M.J. Merwin, D.K. Matlock, Strain partitioning in ultra-fine grained medium-manganese transformation induced plasticity steel, Mater. Sci. Eng. A. 609 (2014) 323–333. doi:10.1016/j.msea.2014.03.120.
- [112] J. Chen, M. Lv, S. Tang, Z. Liu, G. Wang, Correlation between mechanical properties and retained austenite characteristics in a low-carbon medium manganese alloyed steel plate, Mater. Charact. 106 (2015) 108–111. doi:10.1016/j.matchar.2015.05.026.
- [113] D. Hull, D.J. Bacon, Introduction to Dislocations, 5th ed., Butterworth- Heinemann, 2011.
- [114] M.A. Meyers, Dynamic Behavior of Materials, 1994. doi:10.1007/s11340-012-9598-0.
- [115] G.T. (Rusty) Gray, High-Strain-Rate Deformation: Mechanical Behavior and Deformation Substructures Induced, Annu. Rev. Mater. Res. 42 (2012) 285–303. doi:10.1146/annurev-matsci-070511-155034.
- [116] S. Lee, S.J. Lee, B.C. De Cooman, Work hardening behavior of ultrafine-grained Mn transformation-induced plasticity steel, Acta Mater. 59 (2011) 7546–7553. doi:10.1016/j.actamat.2011.08.030.
- [117] I. Choi, S. Lee, D.K. Matlock, J.G. Speer, Strain Control during High Speed Tensile Testing, J.

Test. Eval. 34 (2006) 5–8.

- [118] S. Curtze, V.T. Kuokkala, Dependence of tensile deformation behavior of TWIP steels on stacking fault energy, temperature and strain rate, *Acta Mater.* 58 (2010) 5129–5141. doi:10.1016/j.actamat.2010.05.049.
- [119] G. Frommeyer, U. Brüx, P. Neumann, Supra-Ductile and High-Strength Manganese-TRIP/TWIP Steels for High Energy Absorption Purposes, *ISIJ Int.* 43 (2003) 438–446. doi:10.2355/isijinternational.43.438.
- [120] A. Eisenlohr, I. Gutierrez-Urrutia, D. Raabe, Adiabatic temperature increase associated with deformation twinning and dislocation plasticity, *Acta Mater.* 60 (2012) 3994–4004. doi:10.1016/j.actamat.2012.03.008.
- [121] R. Rana, E. de Moor, J.G. Speer, D.K. Matlock, On the Importance of Adiabatic Heating on Deformation Behavior of Medium-Manganese Sheet Steels, *Jom.* (2018) 1–8. doi:10.1007/s11837-018-2779-2.
- [122] M.H. Cai, W.J. Zhu, N. Stanford, L.B. Pan, Q. Chao, P.D. Hodgson, Dependence of deformation behavior on grain size and strain rate in an ultrahigh strength-ductile Mn-based TRIP alloy, *Mater. Sci. Eng. A.* 653 (2016) 35–42. doi:10.1016/j.msea.2015.11.103.
- [123] R. Alturk, L.G.H. Jr, C.M. Enloe, F. Abu-farha, T.W. Brown, Strain Rate Effect on Tensile Flow Behavior and Anisotropy of a Medium-Manganese TRIP Steel, *JOM.* 70 (2018) 894–905. doi:10.1007/s11837-018-2830-3.
- [124] H.K. Yang, Y.Z. Tian, Z.J. Zhang, Z.F. Zhang, Different strain rate sensitivities between Fe-22Mn-0.6C and Fe-30Mn-3Si-3Al twinning-induced plasticity steels, *Mater. Sci. Eng. A.* 655 (2016) 251–255. doi:10.1016/j.msea.2016.01.003.
- [125] G.I. Taylor, Plastic strain in metals, *J. Inst. Met.* 62 (1938) 307–324.
- [126] Q. Wei, S. Cheng, K.T. Ramesh, E. Ma, Effect of nanocrystalline and ultrafine grain sizes on the strain rate sensitivity and activation volume: Fcc versus bcc metals, *Mater. Sci. Eng. A.* 381 (2004) 71–79. doi:10.1016/j.msea.2004.03.064.
- [127] D. Raabe, H. Springer, I. Gutierrez-Urrutia, F. Roters, M. Bausch, J.B. Seol, M. Koyama, P.P. Choi, K. Tsuzaki, Alloy Design, Combinatorial Synthesis, and Microstructure Property Relations for Low-Density Fe-Mn-Al-C Austenitic Steels, *Jom.* 66 (2014) 1845–1856. doi:10.1007/s11837-014-1032-x.
- [128] S. Brauser, A. Kromm, T. Kannengiesser, M. Rethmeier, In-situ synchrotron diffraction and digital image correlation technique for characterizations of retained austenite stability in low-alloyed transformation induced plasticity steel, *Scr. Mater.* 63 (2010) 1149–1152. doi:10.1016/j.scriptamat.2010.08.007.
- [129] Y. Ma, W. Song, W. Bleck, Investigation of the microstructure evolution in a Fe-17Mn-1.5Al-0.3C steel via in situ synchrotron X-ray diffraction during a tensile test, *Materials (Basel).* 10 (2017). doi:10.3390/ma10101129.
- [130] P.J. Gibbs, B.C. De Cooman, D.W. Brown, B. Clausen, J.G. Schroth, M.J. Merwin, D.K. Matlock, Strain partitioning in ultra-fine grained medium-manganese transformation induced plasticity steel, *Mater. Sci. Eng. A.* 609 (2014). doi:10.1016/j.msea.2014.03.120.